https://doi.org/10.1016/j.actamat.2023.119426

Unraveling the two-stage precipitation mechanism in a hierarchical-structured fcc/L2₁ high-entropy alloy: Experiments and analytical modeling

W. Li[a,b,c], W. Wang[a,b,*], M. C. Niu[c,d], K. Yang[a,b], J.H. Luan[e], H.W. Zhang [a,b,*], Z.B Jiao[c,d,*]

[a] *School of Materials Science and Engineering, University of Science and Technology of China, Shenyang 110016, China*

[b] *Shi-changxu Innovation Center for Advanced Materials, Institute of Metal Research, Chinese Academy of Sciences, Shenyang 110016, China*

[c] *Department of Mechanical Engineering, Research Institute for Advanced Manufacturing, The Hong Kong Polytechnic University, Hong Kong, China*

[d] *The Hong Kong Polytechnic University Shenzhen Research Institute, Shenzhen 518057, China*

[e] *Inter-university 3D Atom Probe Tomography Unit, Department of Materials Science and Engineering, City University of Hong Kong, Hong Kong, China*

[*] *Corresponding authors: wangw@imr.ac.cn (W.W.); hongweizhang@imr.ac.cn(H.W.Z.); zb.jiao@polyu.edu.hk (Z.B.J.)*

Abstract:

Understanding the phase stability and precipitation mechanisms is crucial for engineering multiphase nanostructured alloys with optimal mechanical properties. In this work, we studied the formation and temporal evolution of nanoprecipitates and their effect on mechanical properties of an fcc/$L2_1$ eutectic high-entropy alloy through a combination of experiments and analytical modelling. Aging the alloy at 1023 K results in the precipitation of coherent $L1_2$ nanoparticles in the fcc phase and coherent bcc nanoparticles in the $L2_1$ phase, leading to the formation of an fcc/$L1_2$ + $L2_1$/bcc hierarchical structure. Notably, the scanning transmission electron microscopy (STEM) results reveal that the precipitation in both the fcc and $L2_1$ phases is not through a one-step nucleation, but a two-stage transformation consisting of an initial chemical separation via spinodal decomposition and subsequent structural ordering/disordering. The Gibbs free energy diagrams of the fcc and $L2_1$ phases were modeled through numerical techniques, and the spinodal decomposition regions of the two systems at different temperatures were calculated. Based on the modeling results, we discussed the phase stability and thermodynamics of spinodal decomposition of the two phases. In addition, the formation of hierarchical structure substantially enhances the strength of the alloy. Modeling of the strengthening mechanisms reveals that the order strengthening of $L1_2$ nanoparticles plays a major role in enhancing the yield strength of the alloy, whereas the contribution from the bcc nanoparticles can be negligible. Our findings provide insights into the phase stability, precipitation and strengthening mechanisms of hierarchical-structured alloys.

Keywords: High-entropy alloy; Precipitation; Spinodal decomposition; Strengthening mechanism

1. Introduction

High-entropy alloys (HEAs) have been emerging as a new class of metallic materials, featuring unique microstructure and outstanding mechanical and physical properties [1, 2]. Face-centered cubic (fcc)-type HEAs have attracted considerable attention due to their outstanding toughness and ductility [3, 4]. However, single-phase fcc HEAs have low strengths, which restricts their potential applications in some engineering fields. Considerable efforts have been devoted to improving mechanical strength of fcc HEAs [3, 5-7]. Among them, precipitation strengthening and lamellar structure strengthening have been two of the most effective methods to strengthen fcc HEAs [8-10].

One classical form of precipitation strengthening is the formation of coherent nanoparticles, which leads to the development of high-strength and high-ductility HEAs. For instance, the precipitation of $L1_2$-structured γ' phase in the CoCrFeNi- and CoCrNi-based HEAs significantly enhances the strength of these alloys without causing a significant reduction in ductility [11-15]. Understanding the formation and evolution mechanisms of nanoscale precipitates is critical for optimizing the microstructure and mechanical properties of these HEAs. The multi-component nature of HEAs endows the formation of $L1_2$ precipitates through various mechanisms. It has been extensively investigated how the precipitates develop and evolve in compositionally complexity systems. It is generally understood that the γ' phase can form via the classical nucleation and growth mechanism [16-21]. However, the spinodal decomposition of supersaturated fcc solid solution can also lead to the precipitation of γ' phase in some HEAs [22, 23]. At intermediate temperatures, a miscibility gap exists within the supersaturated fcc solid solution. Because of the interaction between the γ'-forming elements (such as Ni, Al, Ti, and Ta) and non-forming elements (such as Fe, Cr, and Mo), the elemental partitioning through spinodal decomposition leads to the formation of fcc and $L1_2$ phases. For example, Wang *et al.* [24] observed a coherent fcc/$L1_2$ spinodal nanostructure in an $Al_{0.5}Cr_{0.9}FeNi_{2.5}V_{0.2}$ HEA, and the formation mechanism was ascribed to the elemental redistribution of the fcc matrix after the Cr segregation on the deformation bands. The anti-ferromagnetic feature of Cr leads to the compositional instability in systems containing ferromagnetic elements, such as Fe, Co, and Ni [25]. Collins *et al.* [26] and Tan *et al.* [27] reported that γ' phases form via spinodal decomposition instead of the classical nucleation mechanism during the early stages of precipitation in multicomponent superalloys.

Lamellar structure strengthening has been extensively used in eutectic HEAs (EHEAs) consisting of soft and hard lamellar phases. For example, Lu *et al.* [28] developed an $AlCoCrFeNi_{2.1}$ alloy with an fcc/B2 lamellar structure through a casting route. Other types of EHEAs, such as fcc/Laves and fcc/μ lamellar alloys, have also been developed [29, 30]. Because of the existence of high-density lamellar boundaries and hard phases, these EHEAs show significant strength increments as compared with single-phase fcc HEAs. Notably, it was found that aging EHEAs can result in the precipitation of nanoparticles within the eutectic lamellae, leading to the formation of hierarchical structures. For instance, Xiong *et al.* [31] showed that aging an fcc/B2 structured $AlCoCrFeNi_{2.1}$ alloy leads to the formation of an fcc/$L1_2$ and B2/bcc hierarchical structure, which significantly improves the strength of EHEAs. Wang *et al.* [32] also observed the formation of multi-nanoprecipitates in an $AlCr_{1.3}TiNi_2$ EHEA and obtained enhanced mechanical properties.

The precipitation of multiple coherent nanoscale precipitates (CNPs) in EHEAs combines the advantages of the precipitation and boundary strengthening, thus providing a promising strategy to optimize the mechanical properties of EHEAs. Understanding the precipitation mechanisms of CNPs is crucial for tailoring their microstructure and further enhancing the mechanical properties of HEAs. However, the intricate nature of multicomponent multiphase alloys poses significant challenges in comprehending the formation and evolution of CNPs. Particularly, it is controversial how these complex CNPs form and evolve in EHEAs, whether by spinodal decomposition or by the nucleation and growth mechanism, and how they affect the mechanical properties of EHEAs.

The purpose of this paper is to elucidate the precipitation mechanism of nanoparticles in lamellar-structured EHEAs and correlate the precipitate microstructure with mechanical properties. The temporal evolution of the crystal structure, composition, and morphology of CNPs in the dual-phase lamellar structure were systematically investigated by using high-angle annular dark-field scanning transmission electron microscopy (HAADF-STEM), atom probe tomography (APT), and thermodynamic calculations. We show that the formation of CNPs in the two lamellar phases is not through a one-step nucleation, but a two-stage transformation consisting of an initial chemical separation via spinodal decomposition and subsequent structural ordering/disordering. Special attention was paid to understanding the thermodynamic and kinetic characteristics of the two-stage precipitation and its influence on the mechanical properties of the hierarchical-structured EHEAs.

2. Experimental and calculation methods

An alloy with a nominal composition of $(CoCrFeNi)_{87}Al_7Ti_6$ (at.%) was fabricated by arc melting commercial pure raw metals (purity better than 99.9%) in a water-cooled Cu crucible under a high-purity argon atmosphere. The alloy was re-melted five times to ensure chemical homogeneity and then cast into a copper mold with a cavity of 20 × 100 × 6 mm^3. The ingot was homogenized for 4 h at 1373 K, followed by water-quenching. Subsequently, the homogenized sample was aged at 1023 K for 10 min, 4 h, and 24 h, respectively, followed by water-quenching.

Crystal structures were examined by a Bruker AXS D8 Advance X-ray monochromator with Cu $K\alpha$ radiation at a scanning rate of 1.0 °/min in the 2θ range of 20–100°. Electron backscatter diffraction (EBSD) measurements were performed using a FEI XL-30 field-emission scanning electron microscope (SEM) equipped with an EBSD detector. Samples for SEM and EBSD measurements were mechanically polished and electropolished in a 10% oxalic acid aqueous solution at a voltage of 20 V and a current of 0.1 A.

Nanostructures were characterized by a FEI Talos F200X transmission electron microscope (TEM) equipped with selected area electron diffraction (SAED) and energy dispersive spectroscopy (EDS) detectors. TEM foils were mechanically polished to a thickness of 40 μm using SiC paper and then punched into 3-mm-diameter discs and further thinned by twin-jet polishing to a thickness of electron transparency in an electrolyte consisting of perchloric acid (10 vol.%) and ethanol (90 vol.%) at 248 K.

Needle specimens for APT were prepared by the focused ion beam (FIB) lift-out and annular milling method in a FEI Scios FIB/SEM system. The APT analysis was conducted with a CAMECA LEAP ^{TM} 5000XR in voltage mode with a pulse repetition rate of 200 KHz, a pulse fraction of 20%, an evaporation detection rate of 0.2% atom per pulse, and a specimen temperature of 70 K. Integrated Visualization and Analysis Software (IVAS) version 3.8 was used for the 3D reconstruction and analysis.

Dog-bone shaped tensile specimens with a gauge length of 15 mm, a thickness of 1 mm, and a width of 2 mm were cut by electrical-discharge machining. Uniaxial tensile tests were conducted on an Instron 5565 mechanical testing system at room temperature with a strain rate of 10^{-3} s^{-1}. For each condition three samples were tested to ensure the measurement accuracy and reliability.

For the (Co,Cr,Fe,Ni)–Ti–Al system, the binary interaction coefficients were obtained through a simple approximation method proposed by Blazquez *et al.* [33]. The cohesive energy of atomic pairs was calculated using the first nearest-neighbor modified embedded-atom method (1NN MEAM) [34-38]. On the other hand, for the (Ni,Co)–(Cr,Fe)–(Al,Ti) system, the binary interaction coefficients were estimated using the activity coefficient approximation approach, which was calculated using the Thermo-Calc software with the TCHEA4 database (see more details in the Supplementary materials). Inequalities were solved using MATLAB software (version R2017a). The data construction was carried out using a Python script running in Python 3.8.

3. Results

3.1 As-homogenized microstructure

A representative SEM image of the as-homogenized sample is shown Fig. 1a, which reveals a eutectic-like dual-phase structure. The XRD pattern of the sample is shown in Fig. 1b. The peaks at 2θ of 43.46°, 50.56°, and 74.38° correspond to an fcc phase, whereas the minor weak peaks at 2θ of 63.55° and 80.32° are in accordance with the diffraction pattern of a bcc or bcc-derived phase. To analyze the detailed structure of the bcc-structure phase, SAED was used to characterize the lattice structure (see the inset of Fig. 1b, taken along the <011> axis). The crystal structures and the corresponding simulated SAED patterns of bcc, B2, and $L2_1$ lattices along the <011> direction are shown in Supplementary Fig. S1. The presence of the (111) superlattice indicates that the bcc-like phase has an L2_1 structure [31]. The lattice constant of the fcc and L2_1 phases were estimated from the fcc (111) and L2_1 (220) peaks in Fig. 1b, which are 3.6043 and 5.8513 Å, respectively. Figure 1c shows the corresponding elemental distribution of the as-homogenized sample. It is seen that Ti and Al preferentially partition to the L2_1 phase, whereas Cr and Fe partition to the fcc matrix. Ni and Co are roughly uniform in both the L2_1 and fcc phases. The compositions of the fcc and L2_1 phases are summarized in Table 1. The EDS data, together with the XRD and SAED results, indicates that the L2_1 phase is a $(Ni,Co)_2(Al,Ti)$-type phase. The EBSD phase map and inverse pole figure (IPF) map of the as-homogenized sample are displayed in Fig. 1d, from which the volume fractions of the fcc and L2_1 phases were calculated to be 84% and 16%, respectively.

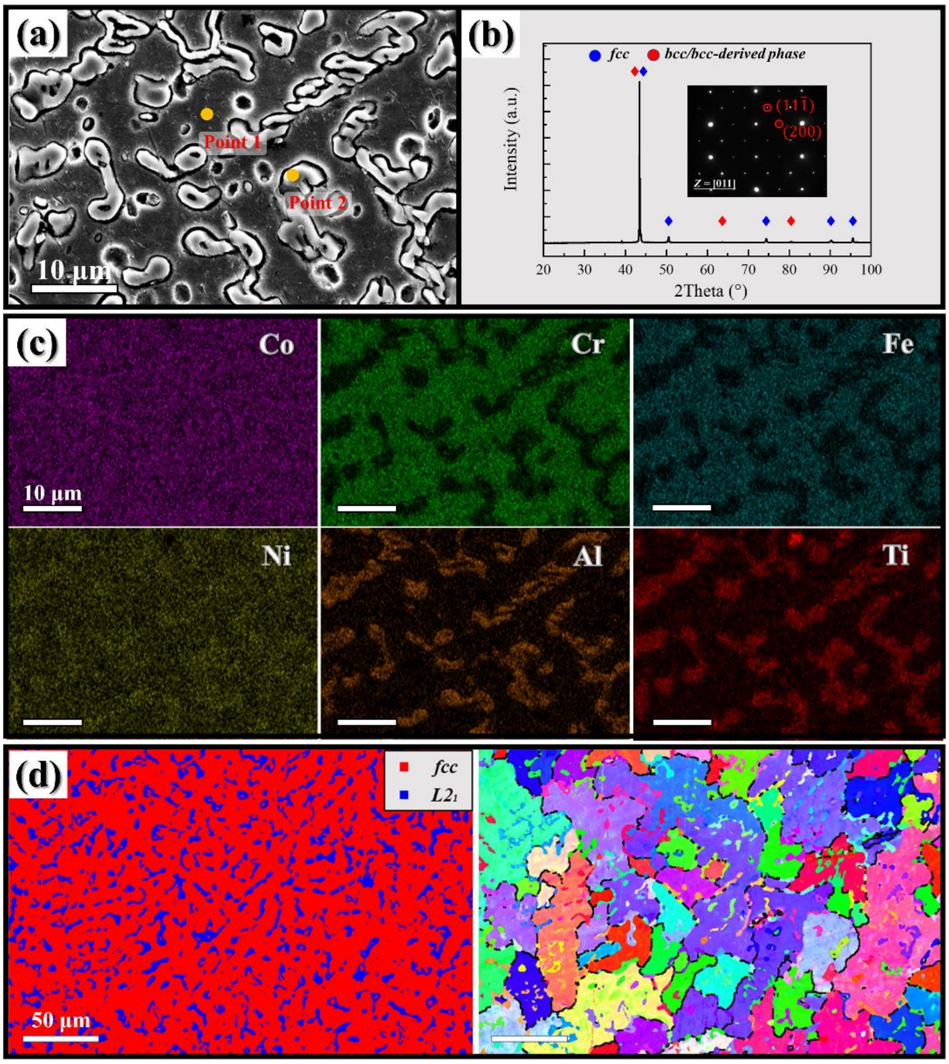

Fig. 1. Microstructure of the as-homogenized sample: (a) SEM micrograph, (b) XRD profile and SAED pattern, (c) elemental distributions corresponding to (a), and (d) phase distribution and IPF maps.

Table 1. Compositions of the fcc and $L2_1$ phases (at.%).

	Co	Cr	Fe	Ni	Al	Ti
fcc	21.74 ± 0.23	25.10 ± 0.21	24.29 ± 0.22	20.37 ± 0.22	4.31 ± 0.16	4.19 ± 0.10
$L2_1$	20.92 ± 0.20	5.48 ± 0.11	7.34 ± 0.13	27.45 ± 0.22	20.94 ± 0.27	17.87 ± 0.16

3.2 Precipitation evolution during aging

3.2.1 Fcc phase

Figures 2a-c depict the TEM morphology and corresponding SAED patterns of the fcc phase after aging at 1023 K for 10 min, 4 h, and 24 h, respectively. In the 10-min aged sample (Fig. 2a), ultrafine nanoparticles are observable, but the SAED pattern still exhibits an fcc single-phase structure without any indication of second phase formation. As the aging time increases to 4 h (Fig. 2b), spherical nanoparticles in the fcc phase grow and become more distinguishable, and the faint superlattice spots suggest that the nanoparticles undergo a structural transition at this aging stage. The size of the nanoparticles further increases as the aging time increases to 24 h (Fig. 2c). The clear superlattice spots and corresponding dark-field (DF)-TEM image confirm that the nanoparticles in the 24-h aged condition possess an $L1_2$ structure.

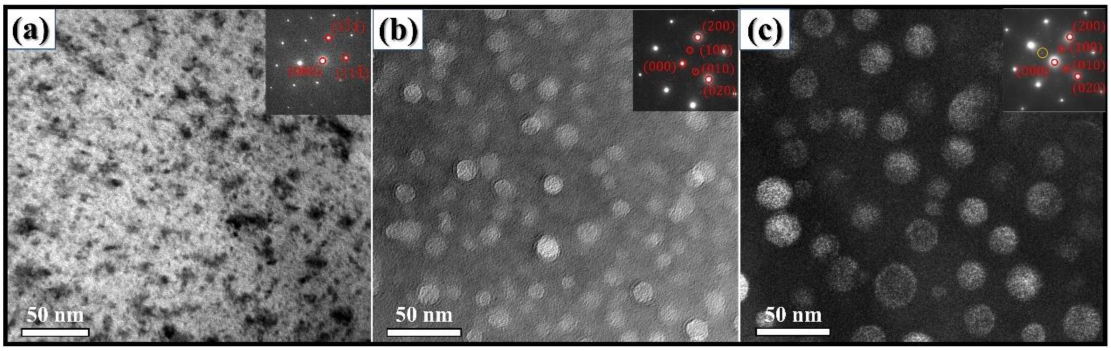

Fig. 2. TEM microstructures of the fcc phase after aging at 1023 K for (a) 10 min (bright-field (BF)-TEM), (b) 4 h (BF-TEM), and (c) 24 h (DF-TEM).

To understand how the crystal structure of the nanoparticles evolves during aging, high-resolution TEM (HR-TEM) was used to analyze the lattices at different aging conditions. Figure 3a shows the microstructure of the 10-min aged sample, which reveals nanoscale regions with different contrasts. The fast Fourier transform (FFT) pattern of this sample (Fig. 3b) shows the absence of any superlattices but the presence of satellite spots, which suggests that the spinodal decomposition of the fcc phase occurs at this stage. Figure 3c displays nanoparticles in the 4-h aged condition, and an enlarged view of a particle in Fig. 3c is illustrated in Fig. 3d. Notably, the FFT patterns (Fig. 3e) reveal that the right half of the particle retains the fcc structure, whereas the left half has transformed to an ordered $L1_2$ structure, which is coherent with the fcc phase. The lattice profiles of the fcc and $L1_2$ phases are displayed in Fig. 3f, which reveals an order transition of the particle at this stage. As the aging time increases to 24 h, the formation of $L1_2$ particles in the fcc matrix is clearly evident. Figure 3g shows an $L1_2$ particle in the 24-h aged condition, and the FFT pattern (Fig. 3h) reveals that it is almost fully ordered. The inverse FFT (IFFT) image in Fig. 3i further confirms that the nanoparticle has a well-defined $L1_2$ structure.

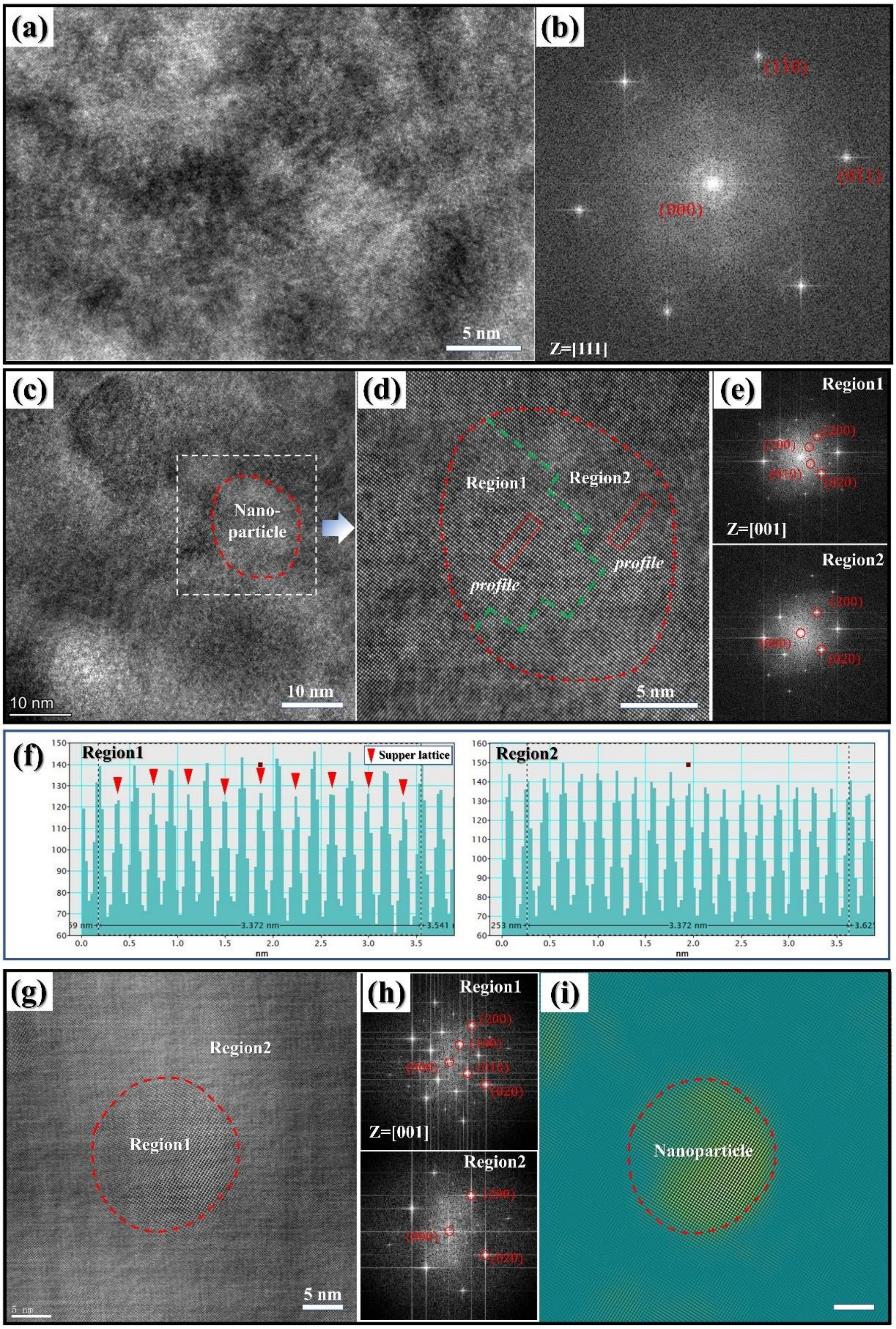

Fig. 3. HR-TEM results showing the structural evolution of the nanoparticles in the fcc phase: (a) HR-TEM image and (b) corresponding FFT pattern of the 10-min aged sample, (c) HR-TEM image and (d) enlarged view of the 4-h aged sample, (e) FFT patterns and (f) lattice profiles of regions 1 and 2 in (d), (g) HR-TEM image and (h) corresponding FFT patterns of the 24-h aged sample, and (i) IFFT image of (g) using the {100} superlattice reflections of the $L1_2$-type nanoparticles.

The microstructural and compositional changes of the nanoparticles in the fcc phase at different aging conditions were probed by HAADF-STEM and EDS mapping, and the results are displayed in Figs. 4a-c. In the 10-min aged condition, nanoparticles with dark contrast are slightly enriched in Ni, Ti, and Al, as shown in Fig. 4a. The average size of the nanoparticles was estimated to be 1.6 ± 0.8 nm. As the aging time increases, the average size of nanoparticles increases to 6.6 ± 1.5 nm at 4 h and 13.0 ± 2.2 nm at 24 h, as displayed in Figs. 4b and c, respectively. Moreover, the enrichment of Ni, Ti, and Al in the spherical nanoparticles became more pronounced with increased aging time, demonstrating a clear time-dependence of particle composition.

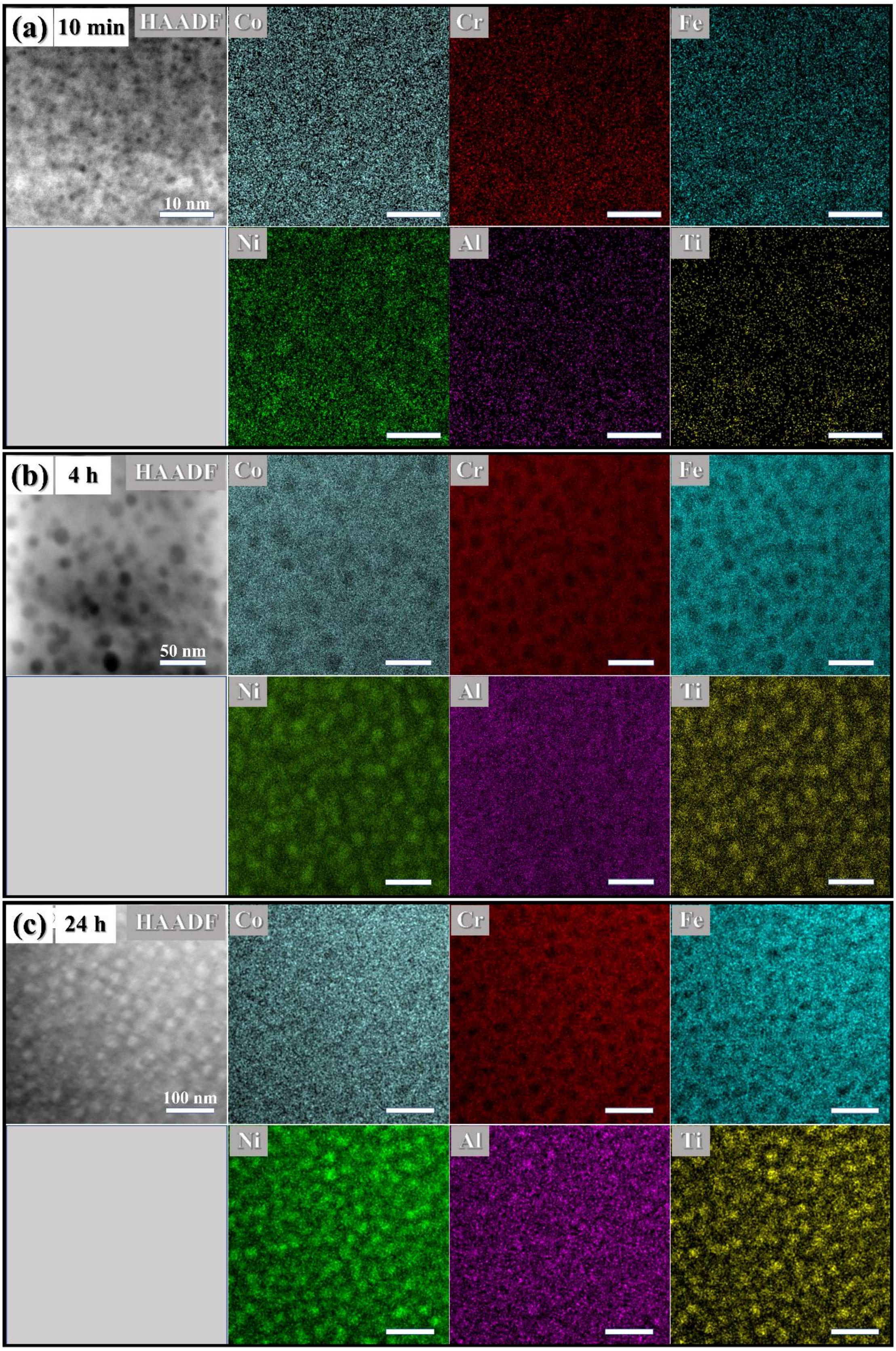

Fig. 4. HAADF-STEM images and elemental mapping of the fcc phase after aging at 1023 K for (a) 10 min, (b) 4 h, and (c) 24 h.

APT was used to quantitatively characterize the compositional evolution of the nanoparticles and matrix of the fcc region with aging time. The atom maps together with the iso-surfaces of the fcc region at the 10-min, 4-h, and 24-h aged conditions are illustrated in Figs. 5a-c, respectively, and the corresponding proximity histograms are displayed in Figs. 5d-f, respectively. The compositions of the nanoparticles and matrix at the three aged conditions are summarized in Table 2. In the 10-min aged condition, the nanoparticles contain 52.23% Ni, 14.36% Co, 17.61% Ti, and 9.55% Al (at.%), together with a small amount of Fe and Cr. As the aging time increases, the concentration of Ni in the nanoparticles increase. At the 24-h aged condition, the atomic ratio of (Ni + Co):(Ti + Al) is close to 3:1, which suggests that the composition of the nanoparticles approaches the stoichiometric ratio of the ordered A_3B-type $L1_2$ phase.

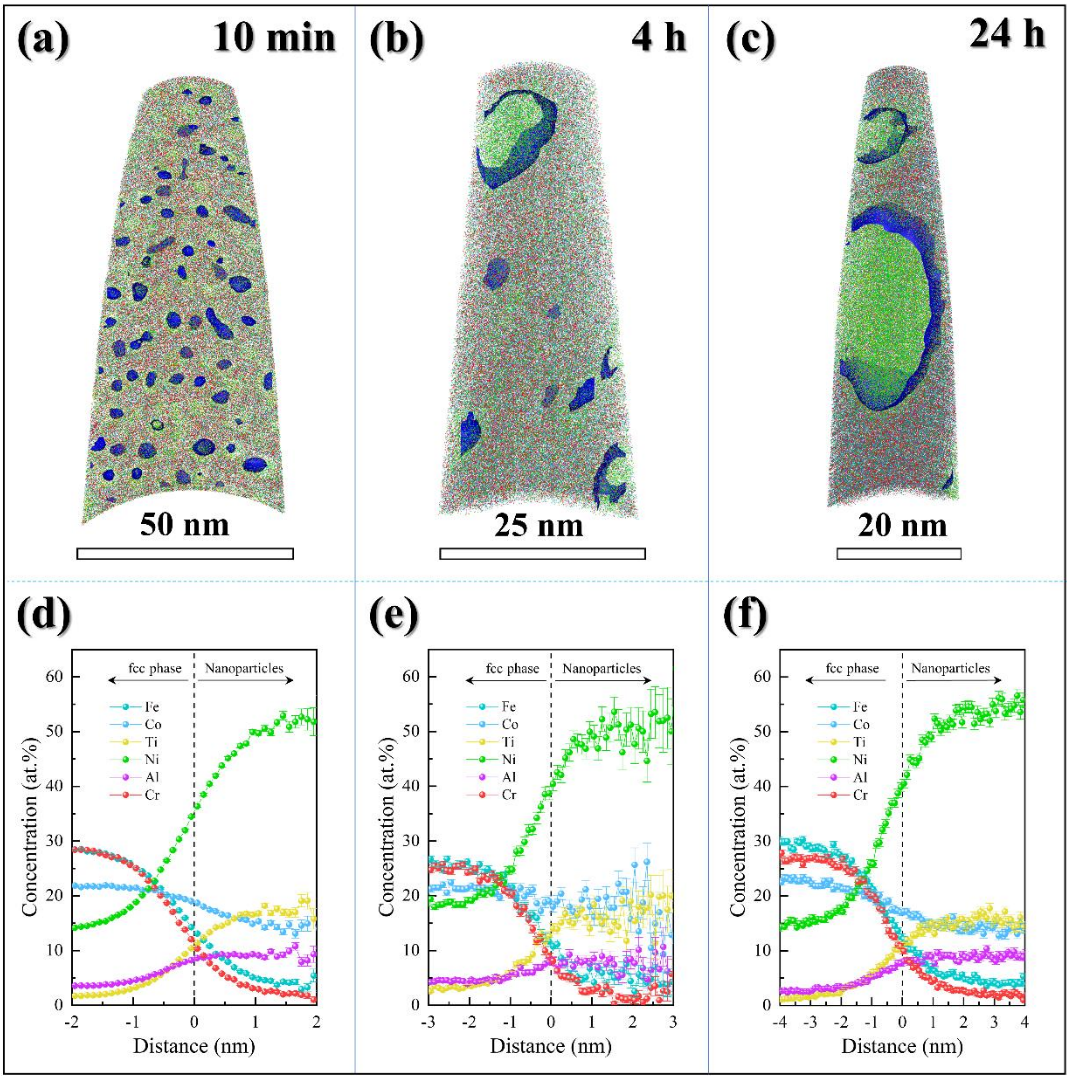

Fig. 5. APT maps, iso-concentration surfaces, and proximity histogram of the nanoparticles in fcc phase after aging at 1023 K for (a, d) 10 min, (b, e) 4 h, and (c, f) 24 h.

Based on the aforementioned results, the fcc phase undergo rapid chemical separation at the early stage of aging, creating solute-enriched zones but without inducing any structural transformation. The observations suggest that this chemical separation might occur via spinodal decomposition. As the aging time increases, the solute-enriched zones undergo an orderly structural transition, and a fully ordered $L1_2$ structure is formed after aging for 24 h. It is important to note that the chemical separation and structural transformation in the fcc phase are not concurrent but sequential.

3.2.2 $L2_1$ phase

TEM morphologies and corresponding SAED patterns of the $L2_1$ phase after aging for 10 min, 4 h, and 24 h are shown in Figs. 6a-c, respectively. The 10-min aged sample exhibits the formation of nanoparticles in the TEM image, but the SAED pattern shows no change of diffraction spots as compared with that in the as-homogenized sample. As the aging time increases to 4 h, the nanoparticles (with dark contrast) in the $L2_1$ phase change to a cuboidal shape and become more visible compared to the 10-min aged sample. At the 24-h aged condition, the size of the cuboidal nano-precipitates increases, and no diffraction spots other than the $L2_1$ phase can be observed from the SAED pattern. The structural evolution of the nanoparticles in the $L2_1$ phase with aging time was examined using HR-TEM, and the results are presented in Figs. 6d-e. In the 10-min aged condition (Fig. 6d), the nanoparticles (Region 2) have the same diffraction pattern as their parental $L2_1$ phase (Region 1), indicating that no structural transformation takes place in these nanoparticles. A representative HR-TEM image and the corresponding FFT patterns of the $L2_1$ phase in the 4-h aged condition are shown in Fig. 6e. Unlike the $L2_1$ phase that have {111} superlattices, the nanoparticles only exhibit the basic diffraction spots of a bcc phase without any superlattice spots, indicating that these nanoparticles in the $L2_1$ phase are disordered bcc particles. Similar observations were reported in an $AlCoCrFeNi_{2.1}$ EHEA, in which Cr-enriched bcc-structured nanoparticles are formed in a B2 phase via spinodal decomposition [31, 39].

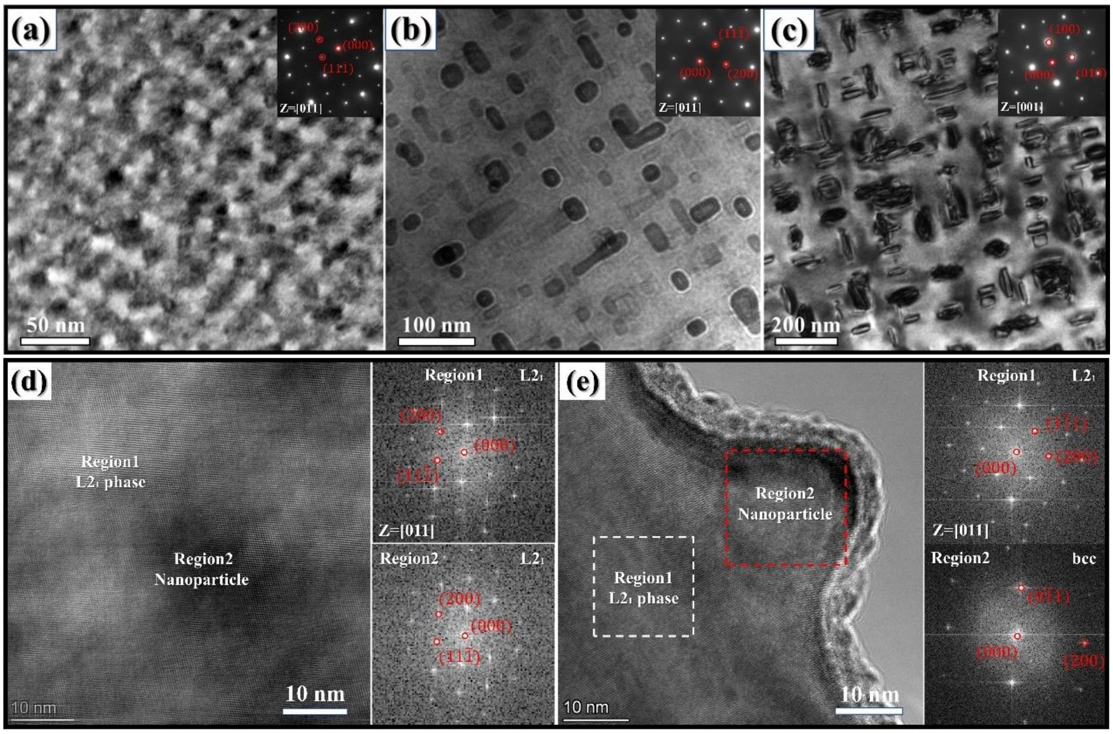

Fig. 6. TEM morphologies and SAED patterns of nanoparticles in the L2_1 phase after aging at 1023 K for (a) 10 min, (b) 4 h and (c) 24 h. HR-TEM images and corresponding FFT patterns of the L2_1 phase in the (d) 10-min and (e) 4-h aged conditions.

The distribution of alloying elements in the L2_1 phase in different aging conditions was characterized using STEM-EDS. The STEM images and corresponding EDS maps of the L2_1 phase in the 10-min, 4-h, and 24-h aged conditions are illustrated in Figs. 7a-c, respectively. The elemental partitioning was clearly observed after aging for 10 min. The nanoparticles are enriched in Cr and Fe, and depleted in Al and Ti. As the aging time increases to 4 and 24 h (Figs. 7b and c, respectively), the Cr/Fe-enriched particles grow, and the enrichment of Cr and Fe becomes more pronounced. These observations suggest that the elemental partitioning and structural transformation of the bcc nanoparticles in the L2_1 phase occur sequentially with aging time, similar to the formation of L1_2 nanoparticles in the fcc phase.

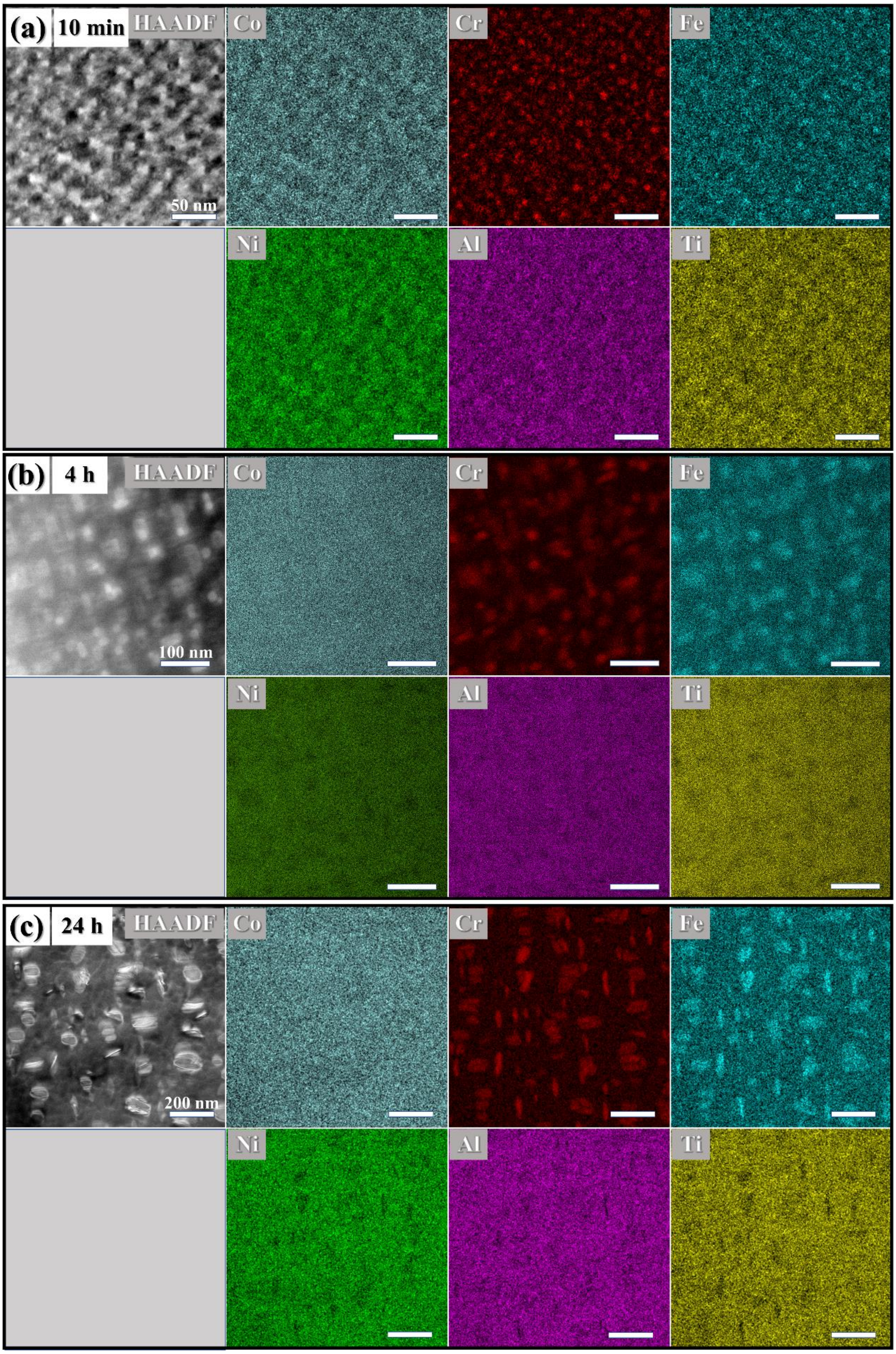

Fig. 7. HAADF-STEM images and EDS mapping of the $L2_1$ phase after aging at 1023 K for (a) 10 min, (b) 4 h, and (c) 24 h.

Table 2. Compositions of different phases in the as-homogenized and aged samples obtained through APT and STEM-EDS.

	Phase	Co	Cr	Fe	Ni	Al	Ti
As homogenized	fcc (C_0_fcc)	21.64 ± 1.55	24.03 ± 1.57	24.93 ± 1.58	20.48 ± 1.43	4.90 ± 0.76	4.02 ± 0.73
	$L2_1$ (C_0_$L2_1$)	25.21 ± 0.78	5.34 ± 0.34	8.14 ± 0.43	33.21 ± 0.43	13.12 ± 0.78	14.98 ± 0.74
10-min aged	Fcc (C_1_fcc)	21.74 ± 0.19	25.72 ± 0.20	26.29 ± 0.20	18.47 ± 0.16	4.56 ± 0.08	3.23 ± 0.06
	CNPs in fcc	14.36± 0.66	2.26 ± 0.28	4.03 ± 0.36	52.23 ± 0.95	9.55 ± 0.55	17.61 ± 0.72
	$L2_1$ (C_1_$L2_1$)	22.18 ± 3.77	4.60 ± 0.78	7.37 ± 1.25	30.28 ± 1.25	17.41 ± 1.84	18.17 ± 3.08
	CNPs in $L2_1$	21.29 ± 3.57	10.24 ± 1.72	8.81 ± 1.49	25.40 ± 4.26	15.40 ± 1.63	18.87 ± 3.16
4-h aged	fcc	22.08 ± 0.51	24.84 ± 0.54	26.70 ± 0.55	19.00 ± 0.49	4.29 ± 0.26	3.10 ± 0.22
	CNPs in fcc	14.76 ± 3.71	3.16 ± 1.81	2.28 ± 2.21	53.54 ± 5.37	8.01 ± 2.84	18.27 ± 4.10
	$L2_1$	23.53 ± 3.05	4.38 ± 3.67	7.15 ± 1.20	29.72 ± 4.98	16.73 ± 1.75	18.49 ± 3.09
	CNPs in $L2_1$	20.78 ± 3.93	15.78 ± 0.74	12.04 ± 2.21	24.13 ± 3.55	13.31 ± 1.21	13.97 ± 1.95
24-h aged	Fcc (C_2_fcc)	23.62 ± 0.57	27.52 ± 0.61	29.88 ± 0.62	14.89 ± 0.49	2.77 ± 0.23	1.33 ± 0.16
	CNPs in fcc	14.19 ± 0.88	1.85 ± 0.34	4.26 ± 0.51	55.44 ± 1.26	9.24 ± 0.73	15.02 ± 0.90
	$L2_1$ (C_2_$L2_1$)	23.43 ± 4.05	2.64 ± 0.48	5.22 ± 0.92	29.35 ± 5.06	19.00 ± 2.12	20.36 ± 3.50
	CNPs in $L2_1$	23.20 ± 3.85	13.39 ± 2.22	11.02 ± 1.83	25.91 ± 4.30	12.94 ± 1.30	13.54 ± 2.24

3.3 Mechanical property

Figure 8 shows the tensile stress-strain curves of the alloy at the as-homogenized and 4-h aged conditions. The yield strength, ultimate tensile strength, and elongation to failure of the as-homogenized sample are 404 ± 8 MPa, 833 ± 11 MPa, and 9.0% ± 1.3%, respectively. Aging for 4 h results in a striking enhancement in the mechanical strength. The aged alloy exhibits a yield strength of 751 ± 6 MPa (~86% increment) and an ultimate tensile strength of 1148 ± 12 MPa (~38% increment) while maintaining a decent ductility, with an elongation-to-failure of 7.0% ± 1.0%. The inset in Fig. 8 shows the strain-hardening rate curves for the as-homogenized and 4-h aged alloys, which possess a similar work-hardening behavior. These observations suggest that the aging treatment substantially improves the mechanical strength of the hierarchical-structured alloys without causing a significant reduction in ductility and strain hardening capability.

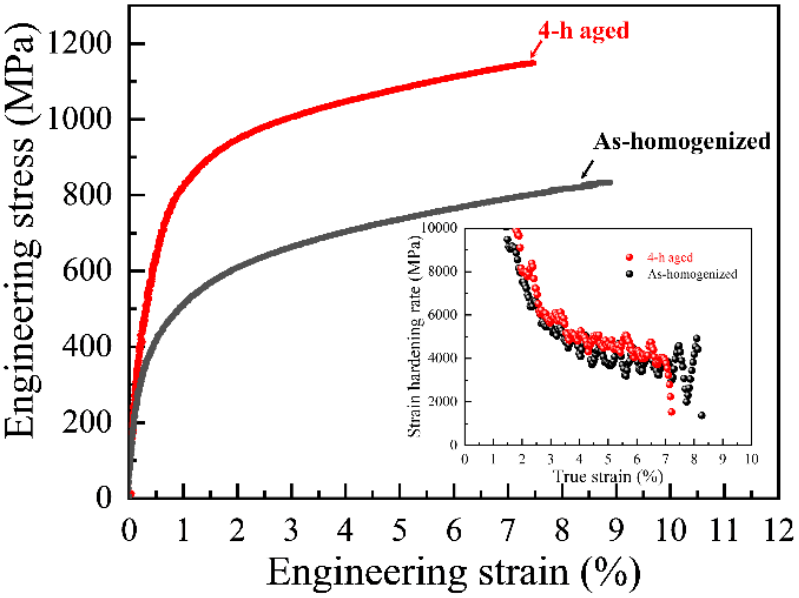

Fig. 8. Tensile stress-strain and strain hardening rate-strain curves of the as-homogenized and 4-h aged samples.

4. Discussion

4.1 Thermodynamic origins of two-stage precipitation

4.1.1 Two-stage precipitation of $L1_2$ from the fcc phase

The aforementioned microstructure results suggest that the $L1_2$ nanoparticles in the fcc phase are formed through a two-stage precipitation involving an initial spinodal decomposition and subsequent structural ordering, rather than a classical nucleation and growth process. To understand the thermodynamic origins of the spinodal decomposition in the fcc phase, we calculate the spinodal decomposition zones at the aging and solutionizing temperatures (1023 and 1373 K, respectively) by solving the thermodynamic criterion for spinodal decomposition. In the fcc system, the transition metals, such as Co, Cr, Fe, and Ni, have similar atomic sizes and tend to form fcc solid solutions [40, 41]. Thus, these four elements were considered as one component in the pseudo-ternary system. Previous studies showed that adding Al and Ti to fcc HEAs would lead to the formation of various types of intermetallic compounds, such as B2-NiAl, η-Ni_3Ti, $L1_2$-$Ni_3(Al,Ti)$, and $L2_1$-Ni_2AlTi [42, 43]. Moreover, it was found that the type and volume fraction of intermetallic phases are highly dependent on the Al and Ti contents and ratio [44]. Consequently, for streamlined calculations, we opted for the

(Co,Cr,Fe,Ni)–Ti–Al pseudo ternary system to evaluate the thermodynamic stability and phase transformations in the fcc phase.

At an initial stage of spinodal decomposition, the system composition fluctuates slightly, and the change of Gibbs free energy of the system before and after the spinodal decomposition can be expressed as [45]

$$\begin{aligned}\Delta G = x[\mu_{(Co,Cr,Fe,Ni)}(x,y) - \mu_{(Co,Cr,Fe,Ni)}(x_0,y_0)] + y[\mu_{Ti}(x,y) - \mu_{Ti}(x_0,y_0)] + \\ z[\mu_{Al}(x,y) - \mu_{Al}(x_0,y_0)]\end{aligned} \tag{1}$$

where x_0 and y_0 are the mole fraction of (Co,Cr,Fe,Ni) and Ti before the composition fluctuation, respectively, and x and y are the mole fraction of (Co,Cr,Fe,Ni) and Ti after the composition fluctuation, respectively. Correspondingly, the mole fractions of Al in the two states are expressed as $z_0=1-x_0-y_0$ and $z=1-x-y$, respectively. $u_i(x,y)$ and $u_i(x_0,y_0)$ (i = (Co,Cr,Fe,Ni), Ti, and Al) are the chemical potential of the i component in the system before and after the composition fluctuation, respectively, which can be given by [46, 47]

$$\mu_{(\mathrm{Co,Cr},Fe,Ni)}(x,y) = G(x,y) + (1-x)\frac{\partial G(x,y)}{\partial x} - y\frac{\partial G(x,y)}{\partial y} \tag{2}$$

$$\mu_{Ti}(x,y) = G(x,y) - x\frac{\partial G(x,y)}{\partial x} + (1-y)\frac{\partial G(x,y)}{\partial y} \tag{3}$$

$$\mu_{Al}(x,y) = G(x,y) - x\frac{\partial G(x,y)}{\partial x} - y\frac{\partial G(x,y)}{\partial y} \tag{4}$$

$$\mu_{(\mathrm{Co,Cr},Fe,Ni)}(x_0,y_0) = G(x_0,y_0) + (1-x_0)\frac{\partial G(x_0,y_0)}{\partial x} - y\frac{\partial G(x_0,y_0)}{\partial y} \tag{5}$$

$$\mu_{Ti}(x_0,y_0) = G(x_0,y_0) - x_0\frac{\partial G(x_0,y_0)}{\partial x} + (1-y_0)\frac{\partial G(x_0,y_0)}{\partial y} \tag{6}$$

$$\mu_{Al}(x_0,y_0) = G(x_0,y_0) - x_0\frac{\partial G(x_0,y_0)}{\partial x} - y_0\frac{\partial G(x_0,y_0)}{\partial y} \tag{7}$$

Substituting Eqs. 2–7 into Eq. 1, we get

$$\Delta G = G(x,y) - G(x_0,y_0) - G_x(x_0,y_0)\delta_x - G_y(x_0,y_0)\delta_y \tag{8}$$

where $G_x(x_0,y_0)$ and $G_y(x_0,y_0)$ are the values at (x_0,y_0) of the first partial derivatives of $G(x,y)$ with respect to x and y, and δ_x and δ_y are the minimum value of component disturbance of (Co,Cr,Fe,Ni) and Ti, respectively, which can be expressed as $\delta_x=x-x_0$ and $\delta_y=y-y_0$, respectively. By ignoring the high order terms, the Gibbs free energy of the system, $G(x, y)$, at (x_0, y_0) can be Taylor expanded as

$$G(x,y) = G(x_0,y_0) + G_x(x_0,y_0)\delta_x + G_y(x_0,y_0)\delta_y + \frac{1}{2}[G_{xx}(x_0,y_0)\delta_x{}^2 + 2G_{xy}(x_0,y_0)\delta_x\delta_y + G_{yy}(x_0,y_0)\delta_y{}^2] \tag{9}$$

where G_{xx} (x_0, y_0), G_{yy} (x_0, y_0), and G_{xy} (x_0, y_0) are the second-order partial derivatives of $G(x,y)$ with respect to x and y at (x_0,y_0), respectively. The change in Gibbs free energy can be obtained by substituting Eq. 9 into Eq. 8

$$\Delta G = \frac{1}{2}[G_{xx}(x_0,y_0)\delta_x{}^2 + 2G_{xy}(x_0,y_0)\delta_x\delta_y + G_{yy}(x_0,y_0)\delta_y{}^2] \tag{10}$$

When $\Delta G<0$, the infinitesimal fluctuation of components in the system would make the system unstable and leads to componential separation, i.e., spinodal decomposition [24, 48-50]. Thus, the criterion of spinodal decomposition in the (Co,Cr,Fe,Ni)–Ti–Al ternary system can be given by

$$[G_{xx}(x_0,y_0)\delta_x{}^2 + 2G_{xy}(x_0,y_0)\delta_x\delta_y + G_{yy}(x_0,y_0)\delta_y{}^2] < 0 \tag{11}$$

The schematic diagram of the composition fluctuation is visualized in the pseudo ternary (Co,Cr,Fe,Ni)–Ti–Al phase diagram shown in Fig. 9a. The ratio between δ_x and δ_y can be expressed by the angle between the compositional fluctuation direction and the (Co,Cr,Fe,Ni) concentration axis, θ, as given by

$$\frac{\delta_x}{\delta_y} = \frac{\sin(60^\circ - \theta)}{\sin\theta} \tag{12}$$

The relationship between δ_x/δ_y and θ is shown in Fig. 9a. Based on the above analyses, we discuss the three situations as follows.

(i) When G_{xx} (or G_{yy})<0, Eq. 11 can be expressed as

$$(\frac{\delta_x}{\delta_y} + \frac{G_{xy}}{G_{xx}})^2 > \frac{G_{xy}{}^2 - G_{xx}G_{yy}}{G_{xx}{}^2} \tag{13}$$

When $G_{xx}{}^2$-$G_{xx}G_{yy}<0$, Eq. 11 always holds. That is, the fluctuation of component x and y in any directions makes $\Delta G<0$, which leads to the spinodal decomposition of the system. In this case, the direction of the composition fluctuation can be arbitrary (θ can be any value in the range of 0–360°).

(ii) When G_{xx} (or G_{yy})<0 and $G_{xx}{}^2$-$G_{xx}G_{yy}>0$, the following conditions are needed to make Eq. 11 hold,

$$\frac{\delta_x}{\delta_y} > -\frac{(G_{xy}{}^2 - G_{xx}G_{yy})^{\frac{1}{2}}}{G_{xx}} - \frac{G_{xy}}{G_{xx}}, \frac{\delta_x}{\delta_y} < \frac{(G_{xy}{}^2 - G_{xx}G_{yy})^{\frac{1}{2}}}{G_{xx}} - \frac{G_{xy}}{G_{xx}} \tag{14}$$

When δ_x/δ_y satisfies Eq. 14, the spinodal decomposition occurs. In this case, the fluctuation directions are not arbitrary, and θ is in a limited range.

(iii) When G_{xx} (or G_{yy})>0 and $G_{xx}{}^2\text{-}G_{xx}G_{yy}>0$, the following condition is needed to make Eq. 11 valid,

$$-\frac{(G_{xy}{}^2-G_{xx}G_{yy})^{\frac{1}{2}}}{G_{xx}}-\frac{G_{xy}}{G_{xx}}<\frac{\delta_x}{\delta_y}<\frac{(G_{xy}{}^2-G_{xx}G_{yy})^{\frac{1}{2}}}{G_{xx}}-\frac{G_{xy}}{G_{xx}} \tag{15}$$

Similar as in case (ii), the fluctuation directions are not arbitrary either, and θ is in a limited range.

According to Ref. [51], assuming that the (Co,Cr,Fe,Ni)–Ti–Al ternary system is a regular solution, the Gibbs free energy can be given by

$$\begin{aligned} G(x,y)&=xG^0_{(Co,Cr,Fe,Ni)}+yG^0_{Ti}+(1-x-y)G^0_{Al}+RT[x\ln x+y\ln y+(1-x-y)\\ &\ln(1-x-y)]+G^E \end{aligned} \tag{16}$$

where G_i^0 (i = (Co,Cr,Fe,Ni), Ti, and Al) are the standard Gibbs free energy of component i, G^E is the excess Gibbs free energy of the fcc system, which is related to the interaction of the components i and j. According to Bragg-Williams model [52], G^E can be expressed as

$$G^E=\sum_{i,j}G^E_{ij}=\sum_{i,j}x_ix_j\Omega_{ij} \tag{17}$$

where $G_{ij}{}^E$ are the excess Gibbs free energy of the i and j system, and Ω_{ij} is the binary interaction coefficient of components i and j. The excess chemical potential, $G_{ij}{}^E$, can be expressed by [53, 54]

$$G^E_{ij}=x_ix_j\Omega_{ij} \tag{18}$$

G_{xx}, G_{yy}, and G_{xy} of the (Co,Cr,Fe,Ni)–Ti–Al system can be given by

$$G_{xx}(x,y)=RT(\frac{1}{x}+\frac{1}{1-x-y})-2\Omega_{(Co,Cr,Fe,Ni)-Al} \tag{19}$$

$$G_{yy}(x,y)=RT(\frac{1}{y}+\frac{1}{1-x-y})-2\Omega_{Ti-Al} \tag{20}$$

$$G_{xy}(x,y)=RT(\frac{1}{1-x-y})+\Omega_{(Co,Cr,Fe,Ni)-Ti}-\Omega_{Ti-Al}-\Omega_{(Co,Cr,Fe,Ni)-Al} \tag{21}$$

According to Refs. [52, 55], Ω_{ij} can be obtained by

$$\Omega_{ij}=zN_A\varepsilon_{ij} \tag{22}$$

where z is the coordination number of the fcc system (the first nearest neighbor), N_A is the Avogadro constant, and ε_{ij} is the atomic interchange energy of component i and j, which is given by

$$\varepsilon_{ij} = u_{ij} - (u_{ii} + u_{ij})/2 \tag{23}$$

where u_{ij}, u_{ii}, and u_{jj} are respectively the cohesive energy of atom pairs denoted by the suffixes. Using the atomic pair cohesive energies provided by the first nearest-neighbor modified embedded-atom method (1NN MEAM) [34-38] and the approximation proposed by Blazquez *et al.* [33], we estimated the cohesive energies between different atomic pairs in the (Co,Cr,Fe,Ni)–Ti–Al pseudo ternary system. Considering the low concentrations of Cr and Fe in the system, we ignored the effect of Cr and Fe and only considered the interaction among Ni, Co, Ti, and Al. The calculated values of u_{ij}, u_{ii} and u_{jj} are shown in Table 3, and the values of u_{ij}, ε_{ij}, and Ω_{ij} for the (Co,Cr,Fe,Ni)–Ti–Al system are listed in Table 4.

Table 3. Calculated cohesive energies (u_{ij}) of atom pairs i and j (*eV/atom*).

i j	Ni	Co	Ti	Al
Ni	–4.44	–4.43	–5.01	–3.91
Co	–	–4.39	–4.19	–3.89
Ti	–	–	–4.73	–4.34
Al	–	–	–	–3.34

Table 4. Calculated cohesive energy (u_{ij}), interchange energies (ε_{ij}), and interaction coefficient (Ω_{ij}) of pseudo binary atomic pairs in the (Co,Cr,Fe,Ni)–Ti–Al system.

Atom pairs	u_{ij} (*eV*)	ε_{ij} (10^{-21} *J*)	Ω_{ij} (*kJ/mol*)
(Co,Cr,Fe,Ni)–(Co,Cr,Fe,Ni)	–4.42	–	–
(Co,Cr,Fe,Ni)–Al	–3.90	–2.42	–17.50
(Co,Cr,Fe,Ni)–Ti	–4.60	–3.90	–28.18
Al–Ti	–4.34	–48.27	–348.79

By solving Eq. 11, the solutions of the inequality (cases (i), (ii), and (iii)) can be visualized as a specific region in the isothermal section of the pseudo-ternary phase diagram [56], which clearly illustrates the spinodal decomposition zone. Figures 9b and c show the spinodal decomposition zone of the (Co,Cr,Fe,Ni)–Ti–Al system at 1023 and 1373 K, respectively. *C_0_fcc* represents the initial composition of the fcc phase in the as-homogenized state, and *C_1_fcc* and *C_2_fcc* are the composition of the fcc phase in the 10-min and 24-h aged states, respectively. It can be seen from Fig. 9b that *C_0_fcc* is within the spinodal decomposition zone at 1023 K, indicating that the spinodal decomposition can occur at this composition. As the aging time increases, the fcc phase undergoes phase separation, and after 10 min of aging, the fcc phase composition (C_1_fcc) starts to evolve toward the non-spinodal decomposition zone. When the aging time reaches 24 h, the fcc phase composition (C_2_fcc) is outside the spinodal decomposition zone, indicating that the composition C_2_fcc is stable at 1023 K. In other words, after aging, the composition moves to the non-spinodal decomposition zone, and the plot of the three compositions shows the direction of the composition evolution towards the equilibrium state. The sectoral range of fluctuating directions for the initial composition C_1_fcc, indicated by the red arrows in Fig. 9b, exhibits fluctuations toward the directions of increasing the Ti and Al concentrations, suggesting that the formation of Ti/Al clusters during the early stages of aging plays a key role in the instability of the system. Additionally, temperature has a significant effect on the spinodal decomposition, as shown in Fig. 9c. When the temperature is increased to 1373 K, the spinodal decomposition region is further reduced, resulting in the C_0_fcc component being located outside the spinodal decomposition zone. The calculated G_{ij} and the fluctuation angle ($\Delta\theta$) of the three compositions at 1023 K are listed in Table 5. The composition C_1_fcc has a lower $\Delta\theta$ value than the initial composition (C_0_fcc), indicating that C_1_fcc is more stable as a consequence of the lower Ti/Al contents. The formation of the fcc + $L1_2$ dual-phase field in the (Co,Cr,Fe,Ni)–Ti–Al system with different (Ti + Al) contents was calculated by using Thermo-Calc with the TCHEA4 database. The calculated pseudo binary (Co,Cr,Fe,Ni)–(Ti + Al) phase diagram is shown in Fig. 9d, in which the spinodal decomposition zone is highlighted with orange. The dash lines are the boundaries of the spinodal decomposition zone, within which the compositions are unstable and spinodal decomposition would occur. The Gibbs free energy of the (Co,Cr,Fe,Ni)–Ti–Al concentration triangle was estimated using the provided interaction coefficients (ignoring the standard Gibbs energy terms for each component), as shown in Fig. 10a. The resulting surface exhibits a concave-upward shape, with susceptibility to changes in the Ti/Al components. The Gibbs free energy and dG/dx change with (Ti + Al) concentration were visualized using two-dimensional curves, as shown in Fig. 10b. The curves demonstrate a clear miscibility gap that verifies the susceptibility to spinodal decomposition when the (Ti + Al) mole fraction exceeds 0.075.

Additionally, Kadirvel *et al.* [57] formulated a CALPHAD framework utilizing the Hessian of free energy to investigate the stability of solid solutions in HEAs. Their methodology yielded dependable predictions. To further validate the stability of the fcc system, we adopted the approach put forth by Kadirvel *et al.* Calculations of eigenvalues and eigenvectors for the C_0_*fcc*, C_1_*fcc*, and C_2_*fcc* compositions were conducted using the Thermo-Calc software with TCHEA4 database. Detailed results are presented in Fig. 11. As depicted in Fig. 11a, projections based on eigenvalues suggest an unstable state for the C_0_*fcc*, C_1_*fcc*, and C_2_*fcc* compositions, signifying a predisposition for spinodal decomposition. Moreover, the critical temperature of decomposition decreases as the decomposition proceeds, indicating gradual system stabilization. Kadirvel *et al.* argued that in the early stage of the spinodal decomposition, elements with the same sign eigenvector components (i.e., positive, or negative) will partition together. The eigenvector results of C_0_*fcc* shown in Fig. 11b reveal compositional separation, specifically between Ni/Al/Ti and Co/Cr/Fe, occurring at temperatures below 1252 K. This result suggests a pseudo-binary behavior within the fcc system. Remarkably, the predicted decomposition direction aligns precisely with the sectoral fluctuation directions calculated using the (Co,Cr,Fe,Ni)–Ti–Al pseudo ternary system. These findings provide strong confirmation of the thermodynamic instability inherent in the fcc system.

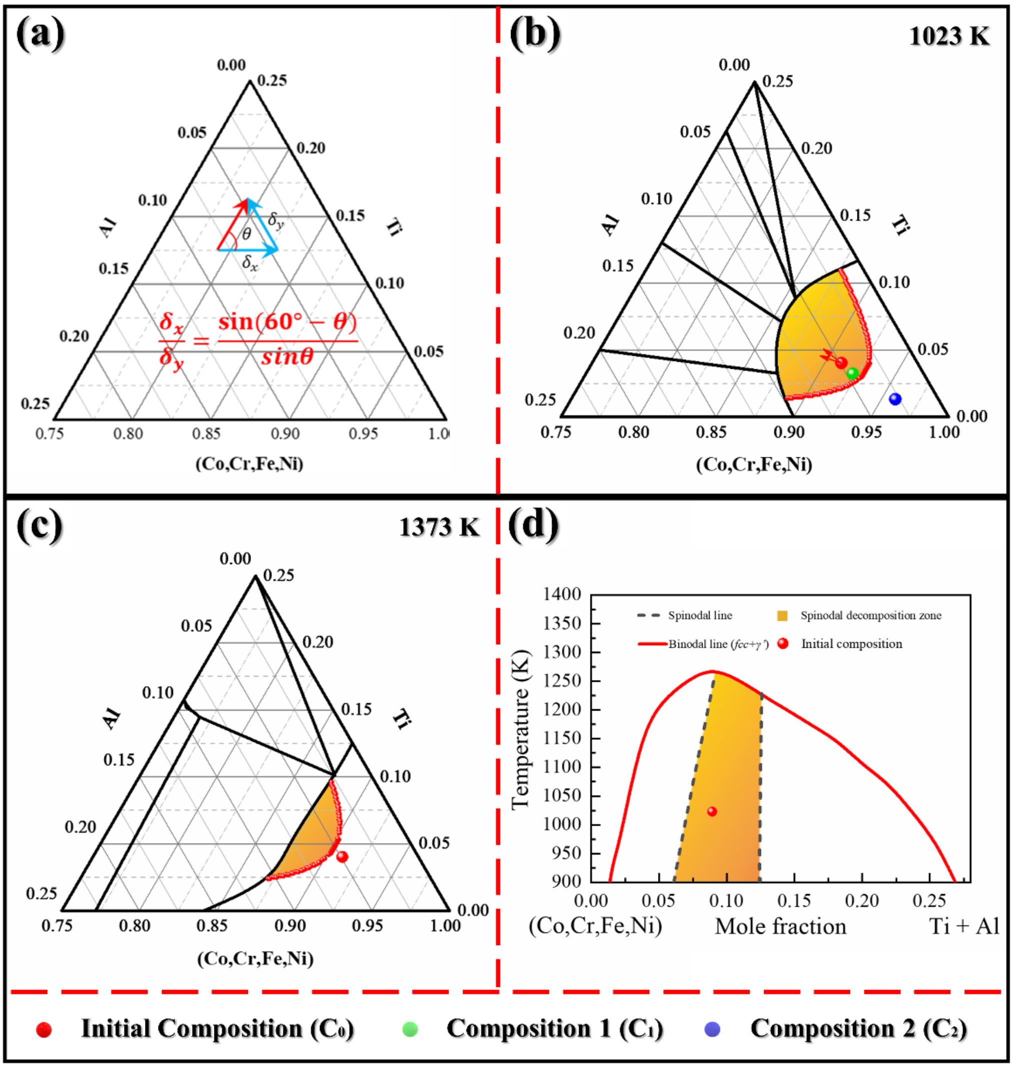

Fig. 9. (a) Schematic diagram of composition fluctuation in the pseudo ternary (Co,Cr,Fe,Ni)–Ti–Al system, the isothermal sections of the system at (b) 1023 and (c) 1373 K, and (d) calculated (Co,Cr,Fe,Ni)–(Ti + Al) pseudo binary phase diagram showing the spinodal decomposition zone.

Table 5. G_{ij}, θ, and $\Delta\theta$ values of the compositions C_0_fcc, C_1_fcc, and C_2_fcc at 1023 K.

Composition	G_{xx} (10^5 J/mol)	G_{yy} (10^5 J/mol)	G_{xy} (10^5 J/mol)	δ_x/δ_y	θ (deg)	$\Delta\theta$ (deg)
C_0	2.18	10.83	5.12	−1.61 −3.09	142.04 161.49	19.45
C_1	2.31	11.47	5.25	−1.83 −2.72	146.93 158.66	11.73
C_2	3.51	16.44	6.45	Nan Nan	Nan Nan	Nan

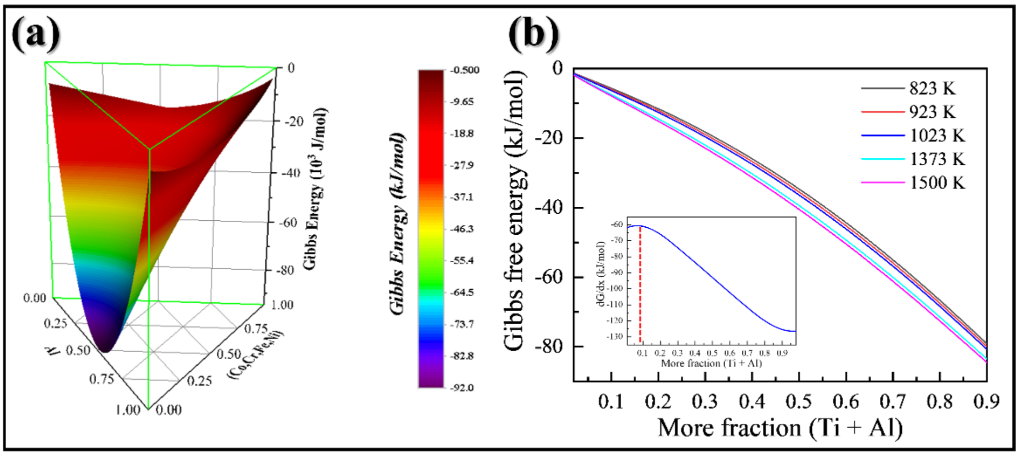

Fig. 10. (a) Gibbs free energy surface of the (Co,Cr,Fe,Ni)–Ti–Al concentration triangle, and (b) Gibbs free energy and dG/dx as a function of (Ti + Al) molar fraction at different temperatures.

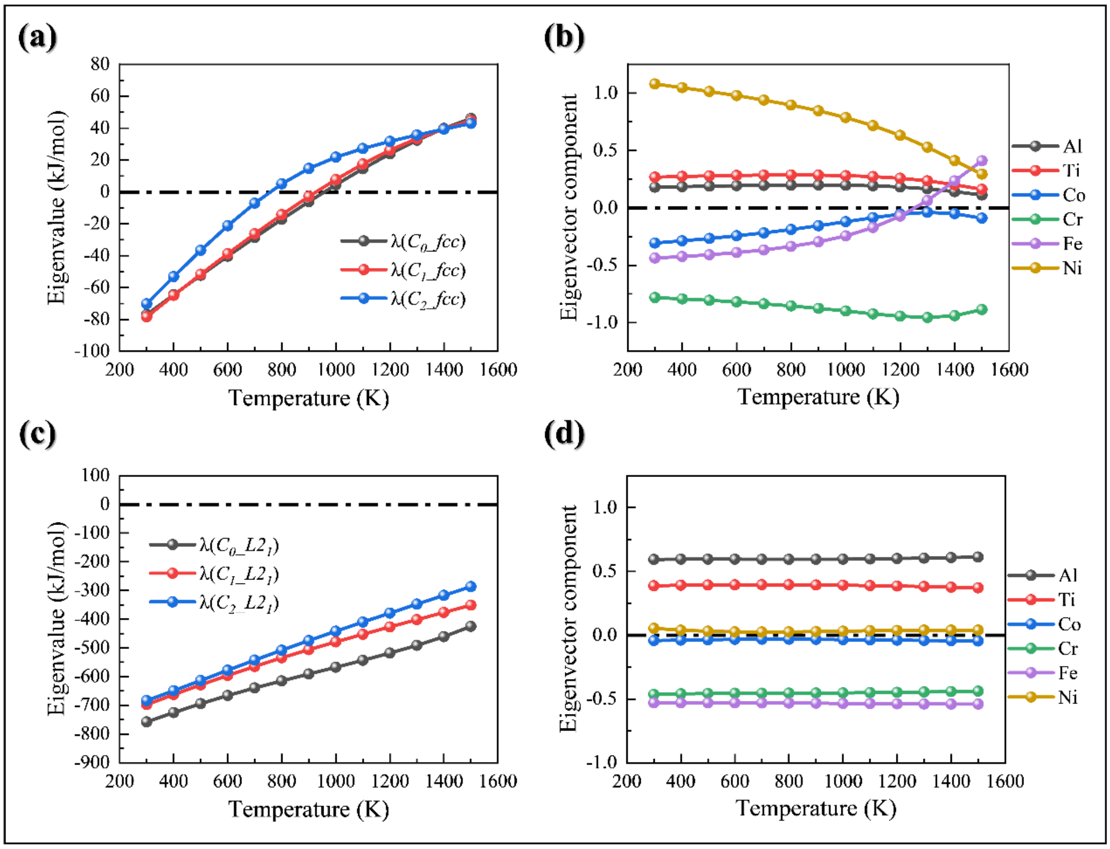

Fig. 11 Eigenvalues and eigenvectors of the (a, b) fcc and (c, d) $L2_1$ system.

The thermodynamic analysis indicates that the spinodal decomposition occurs in the fcc phase in the initial stage of aging. In this stage, thermal vibrations cause fluctuations in the composition of local regions, which are especially pronounced in HEAs, as described as concentration waves by Ding *et al.* [58]. From the thermodynamic point of view, these fluctuations result in the phase separation of the fcc phase. Similar results have been observed in high-temperature superalloys and Al alloys [59, 60]. As the aging time increases to 4 h, the nanoparticles become ordered and transform into the ordered $L1_2$ phase (Figs. 4c-f). Therefore, the chemical separation and structural ordering processes are not simultaneous but sequential in the formation of nanoparticles in the fcc phase.

4.1.2 Two-stage precipitation of bcc particles in the $L2_1$ phase

As with the fcc system, we undertook the simplification of the $L2_1$ system into a pseudo-ternary representation for computational efficiency. Within the $L2_1$ lattice, Co and Ni are interchangeable at the cube corners, whereas Al and Ti occupy the body centers [61], providing a reasonable grouping strategy. Additionally, our observation of synergistic Cr/Fe precipitation during aging justified the grouping of Cr/Fe. Thus, we opted to streamline the $L2_1$ system into a (Ni,Co)–(Cr,Fe)–(Al,Ti) pseudo-ternary system. To gain insight into the thermodynamic origins of spinodal decomposition in the $L2_1$ phase, we calculated the Gibbs free energy of the (Ni,Co)–(Cr,Fe)–(Al,Ti) pseudo-ternary system at 1023 K. The calculation method is similar as that used in the fcc phase in Section 4.1.1, and thus, the calculation details are presented in the Supplementary material. The calculated interaction coefficients of the system, Ω_{ij}, are shown in Table 6. The Gibbs free energy of the (Ni,Co)–(Cr,Fe)–(Al,Ti) concentration triangle was calculated by utilizing the interaction coefficients in Table 6, and the results are shown in Fig. 12a. The energy surface shows a fluctuation of Gibbs free energy in the (Cr,Fe) direction, which was further confirmed by calculating the Gibbs free energy curves as a function of (Cr + Fe) molar fraction at various temperatures, as presented in Fig. 12b. The results show a clear miscibility gap at the (Cr + Fe) molar fraction below 0.3, indicating that the system has a propensity for spinodal decomposition when the mole fraction of (Cr + Fe) is less than 0.3. By applying the spinodal decomposition criterion (Eq. 11), the direction angles of spinodal decomposition of the $L2_1$ phase in the as-homogenized and aged states were calculated, and the results are listed in Table 7. The fluctuation angles (θ) are close to 120°, indicating that the fluctuation of the (Cr,Fe) composition is the primary factor leading to the instability of the system. In other words, the formation of Cr/Fe clusters at the beginning of aging is the key factor causing the instability of the system. As the Cr/Fe concentration decreases in the (NiCo)–(CrFe)–(AlTi) system, the $\Delta\theta$ value gradually decreases, indicating a reduced instability of the system. However, different from the situation in the fcc phase that appears to become stabilized with aging time, the $L2_1$ phase remains susceptible to spinodal decomposition even after 24 h of aging.

We also assessed the stability of the $L2_1$ phase using the framework outlined by Kadirvel *et al.* Eigenvalues and eigenvectors of the $L2_1$ system were computed for the as-homogenized state ($C_0\_L2_1$), the 10-min aging state at 1023 K ($C_1\_L2_1$), and the 24-h aging state ($C_2\_L2_1$), as depicted in Figs. 11c and 11d. The existence of negative eigenvalues spanning the temperature range from 300 K to 1500 K indicates the inherent instability of the $L2_1$ system, implying the favorable thermodynamic conditions for spinodal decomposition. An assessment of eigenvectors for the as-homogenized state reveals an obvious pseudo-binary compositional separation of Al/Ti and Cr/Fe, and partitioning in Ni and Co can be negligible. These predictions are in agreement with our computational and experimental results.

Table 6. Calculated values of Ω_{ij} at 1023 K by using the activity coefficient approximation approach.

Atom pairs	Ω_{ij} (*kJ/mol*)
(Ni,Co)–(Al,Ti)	-327.75
(Cr,Fe)–(Al,Ti)	-401.47
(Ni,Co)–(Cr,Fe)	58.98

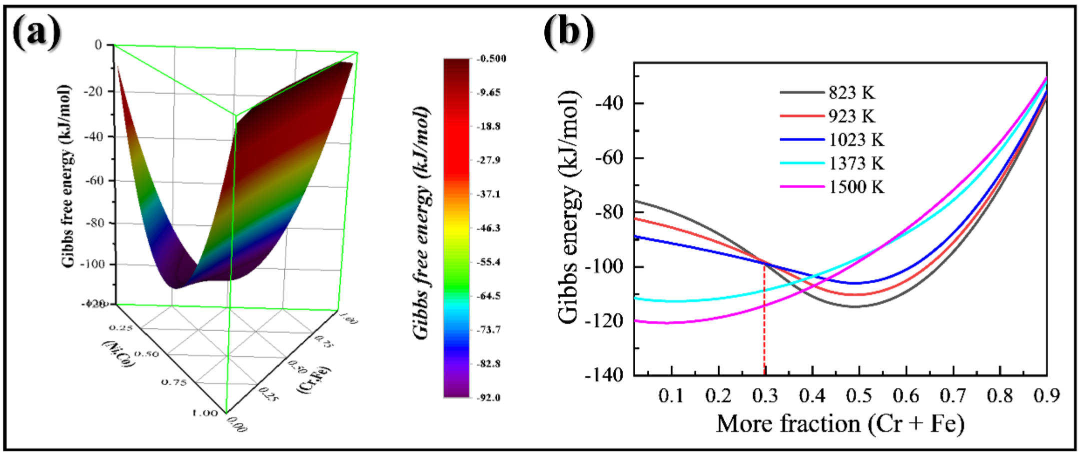

Fig. 12. (a) Gibbs free energy surface of the (Ni,Co)–(Cr,Fe)–(Al,Ti) concentration triangle, and (b) Gibbs free energy as a function of (Cr + Fe) molar fraction at different temperatures.

Table 7. G_{ij}, θ and $\Delta\theta$ values of the $L2_1$ phase in the as-homogenized, 10-min aged, and 24-h aged states.

Conditions	G_{xx} (10^5 J/mol)	G_{yy} (10^5 J/mol)	G_{xy} (10^5 J/mol)	δ_x/δ_y	θ (deg)	$\Delta\theta$ (deg)
As-homogenized	7.00	8.96	8.18	−0.88	113.44	24.57
				−1.46	138.00	
10-min aged	6.96	8.98	8.13	−0.90	114.73	22.49
				−1.44	137.22	
24-h aged	6.93	9.33	8.10	−1.03	121.46	11.49
				−1.31	132.96	

Thermodynamic analysis of the (Ni,Co)–(Cr,Fe)–(Al,Ti) pseudo-ternary system shows that in the early stage of aging, the $L2_1$ phase exhibits a phase separation via spinodal decomposition, which leads to the formation of Cr/Fe-rich nanoparticles with an $L2_1$ structure. As the aging time increases, the increased concentration of Cr and Fe promotes the structural disordering, leading to the transformation of $L2_1$ nanoparticles into bcc-structured disordered nanoparticles. Similar cases were observed in the $AlCoCrFeNi_{2.1}$ [39], $Al_{1.5}CoCrFeNi$ [62], and AlCoCrCuFeNi [63] EHEAs, in which nanoparticles are formed also through the compositional modulation mechanism.

As a result, the precipitation mechanisms in the fcc and $L2_1$ phases can be schematically illustrated in Fig. 13. The precipitation process in the fcc phase can be summarized as

Supersaturated fcc solid-solution → fcc′ + fcc nanoparticles enriched in Ni, Ti, and Al→ fcc′ + $L1_2$-$Ni_3(Al,Ti)$

The process consists of two stages. (1) The spinodal decomposition stage: in the early stage of aging, the spinodal decomposition of the supersaturated fcc solid solution results in the formation of nanoparticles enriched in Ni, Ti and Al, which retain the fcc structure. (2) The structural ordering stage: as the nanoparticles grow, the concentrations of Ni, Ti and Al increase. When the ratio of Ni, Ti, and Al in the nanoparticles approaches the stoichiometric ratio of $L1_2$-type γ' phase, the structure-ordering occurs in the nanoparticles. In other words, the growth of nanoparticles provides the chemical condition for the ordering transformation of the $L1_2$ phase.

Similarly, the precipitation mechanism of the $L2_1$ phase can be summarized as

Supersaturated $L2_1$ phase→ $L2_1'$ + $L2_1$ nanoparticles enriched in Cr and Fe → $L2_1'$ + bcc-(Cr,Fe)

The precipitation process also involves two stages. (1) The spinodal decomposition stage: the spinodal decomposition occurs in the supersaturated $L2_1$ phase, leading to the formation $L2_1$ structured nanoparticles enriched in Cr and Fe. (2) The structure-disordering stage: as the nanoparticles grow, the increased enrichment of Cr and Fe promotes the transformation of nanoparticles from the ordered $L2_1$ to disordered bcc structure.

Kadirvel *et al.* [64] explored the phase transformation pathways in high-entropy alloys (HEAs) through high-throughput phase-field simulations of 36 different HEAs and identified a two-step transformation process involving spinodal decomposition followed by structural ordering/disordering. Our observations coincide with these simulations. This consistency emphasizes the commonality of the phase transformation mechanisms in different HEAs, highlighting the fundamental nature in these alloy systems. However, our study also provides a unique perspective by experimentally demonstrating the existence of such two-step transformation in our particular system. By unraveling the complexity of these transitions, our study paves the way for the controlled regulation of nanophases in HEAs, opening up the possibility of optimizing their mechanical properties and advancing materials engineering.

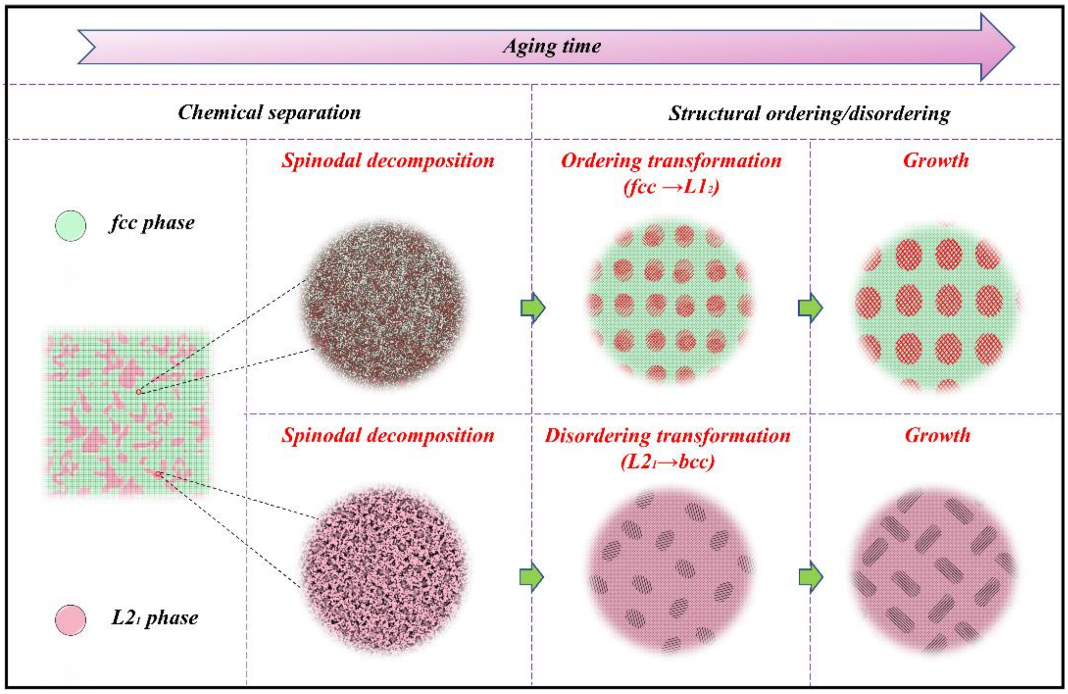

Fig. 13. Schematic diagram of precipitation mechanism in the fcc and $L2_1$ phases.

4.2 Strengthening mechanism

The mechanical results reveal that the yield strength of the 4-h aged sample is significantly improved compared to that of the as-homogenized one, by approximately 86%. This can be attributed to the precipitation of nanoparticles in the fcc and/or $L2_1$ phases, which hinder the movement of dislocations. For the hierarchical-structured alloy, we separately analyze the contribution of the $L1_2$ nanoparticles in fcc phase and the bcc nanoparticles in the $L2_1$ phase.

We first evaluate the influence of the $L1_2$ particles in the fcc phase on the strength of the alloy. Generally, the particle shearing mechanism is operative for nanoparticles with small sizes and having coherent interfaces with the matrix , and the transition from the particle shearing to Orowan bypass mechanism occurs when the nanoparticle size exceeds a critical value or when the particles are incoherent with the matrix [65]. In this work, considering the coherent relationship between the $L1_2$ nanoparticles and fcc matrix and their small size (~6.6 nm), the shearing mechanism is considered to be operative. For the particle shearing mechanism, the increase in yield strength results from the contribution of coherency strengthening ($\Delta\sigma_{cs}$), modulus mismatch strengthening ($\Delta\sigma_{ms}$), and ordering strengthening ($\Delta\sigma_{os}$) [65]. The former two contributions ($\Delta\sigma_{cs}$ and $\Delta\sigma_{ms}$) occur before the dislocations shear the precipitates and the latter occurs during shearing. As a result, the total contributions by shearing precipitates is the larger of ($\Delta\sigma_{cs}$ +$\Delta\sigma_{ms}$) and $\Delta\sigma_{os}$ [66]. According to Refs. [65, 67, 68], the $\Delta\sigma_{cs}$, $\Delta\sigma_{ms}$, and $\Delta\sigma_{os}$ can be evaluated by

$$\Delta\sigma_{cs} = M\alpha_{\varepsilon}(G\varepsilon_c)^{\frac{3}{2}}\left(\frac{rf}{0.5Gb}\right)^{\frac{1}{2}} \tag{24}$$

$$\Delta\sigma_{ms} = 0.0055M(\Delta G)^{\frac{2}{3}}\left(\frac{2f}{G}\right)^{\frac{1}{2}}\left(\frac{r}{b}\right)^{\frac{3m}{2}-1} \tag{25}$$

$$\Delta\sigma_{os} = 0.81M\frac{\gamma_{APB}}{2b}\left(\frac{3\pi f}{8}\right)^{1/2} \tag{26}$$

where M = 3.06 is the Taylor factor, α_{ε} = 2.6 is a lattice-dependent constant [65, 67], $\varepsilon_c=2/3\varepsilon$ is the constrained lattice parameter mismatch, with $\varepsilon=\Delta a/a$ (a is the lattice parameter of the fcc matrix, Δa is the difference between $L1_2$ and fcc phases), G = 78.5 GPa is the shearing modulus of the fcc phase [69], b = 0.255 nm is the magnitude of Burgers vector, ΔG = 11.7 GPa is the shearing modulus mismatch between the precipitates (G_p) and matrix (G) [31], r = 6.6 nm is the mean radius of the precipitates,

f = 12.3% is the volume fraction of precipitates, m = 0.85 is a constant [65], γ_{APB} is the anti-phase boundary (APB) energy of the ordered $L1_2$ phase. Vittori and Mignone [70] established a correlation between the APB energy and Ti/(Ti + Al) ratio for $L1_2$ precipitates. The Ti/(Ti + Al) ratio in the $L1_2$ nanoparticles was determined to be 0.69, and accordingly an APB energy of 190 mJ/m^2 was employed for the current alloy. The strengthening contributions from the coherency strengthening, modulus mismatch strengthening, and ordering strengthening were estimated to be ~33, ~93, and ~353 MPa, respectively, as summarized in Fig. 14. The overall strength increment resulting from the nanoparticles was thus estimated to be ~353 MPa.

We now analyze the influence of the bcc nanoparticles in the $L2_1$ phase on the strength of the alloy. To understand whether the bcc nanoparticles soften or harden the $L2_1$ phase, we fabricated a model alloy with the same composition as the initial $L2_1$ phase and aged the alloy at 1023 K. The hardness of the model alloy as a function of aging time is presented in Supplementary Fig. S3. It is evident that the hardness of the alloy increases with increased aging time, indicating that the precipitation of disordered bcc nanoparticles enhances the hardness of the $L2_1$ phase. Tian *et al.* [71] observed similar phenomenon in a NiAl alloy, and they found that the increase in strength is not due to the development of disordered bcc nanoparticles, but rather to the lattice change of the B2 phase, because the desolvation of Cr results in the generation of extra vacancies and changes the atomic occupancy and stoichiometry of the B2 phase. Therefore, the hardness increase in our $L2_1$ model alloy can be attributed to changes in the occupancy and stoichiometry of the $L2_1$ phase, induced by the desolvation of Cr/Fe, rather than the Cr/Fe phase itself. In this study, the $L2_1$ phase can be considered a precipitated phase within the fcc matrix, and its ultrahigh hardness and coarse sizes suggest that the $L2_1$ phase strengthens the alloy through the Orowan bypass mechanism [72]. Because the strengthening effect of the Orowan mechanism does not relate to the intrinsic mechanical properties of the precipitates [73], the enhanced hardness of the $L2_1$ phase due to the precipitation of bcc nanoparticles would not change the strengthening efficiency of the $L2_1$ phase. Following an EBSD analysis of the 4-h aged sample (Supplementary Fig. S4), it is evident that the volume fraction and size of the $L2_1$ phase do not have a significant change after aging. As a result, the strengthening effect of the $L2_1$ phase on the hierarchical-structured alloy would not change. Therefore, the influence of the precipitation of bcc nanoparticles in the $L2_1$ phase on the strength of the alloy can be neglected.

On the basis of the above analysis, the strength enhancement of the alloy after aging for 4 h at 1023 K is due to the precipitation of $L1_2$ nanoparticles in the fcc phase. The strengthening contribution from the $L2_1$ phase, $\Delta\sigma_{L21}$, does not change before and after the aging treatment. Consequently, the strength increment after aging for 4 h at 1023 K can be calculated by [74]

$$\Delta\sigma = \sqrt{\Delta\sigma_{L1_2}{}^2 + \Delta\sigma_{L2_1}{}^2} - \Delta\sigma_{L2_1} \tag{27}$$

By employing the Orowan bypass mechanism, the strengthening contribution of the $L2_1$ phase can be calculated by [73]

$$\Delta\sigma_{L2_1} = M\frac{0.4Gb}{\pi\sqrt{1-v}}\frac{\ln(2r_m/b)}{\lambda_p} \tag{28}$$

where G is the shearing modulus of the fcc phase, b is the magnitude of Burgers vector, v = 0.25 is the Poisson ratio, $r_m = \sqrt{2/3}r$ is the mean radius of circular cross-section in a random plane for spherical precipitate [75], $\lambda_p = 2rm(\sqrt{\pi/4f} - 1)$ is the inter-precipitate spacing [76]. The mean radius (r) and volume fraction (f) of the $L2_1$ phase were determined as 2.1 μm and 16%, respectively, based on the SEM and EBSD results shown in Fig. 1. The calculated strength increment after aging for 4 h (compared to the as-homogenized sample) was found to be ~333 MPa, which is in good agreement with the experimental value (~347 MPa).

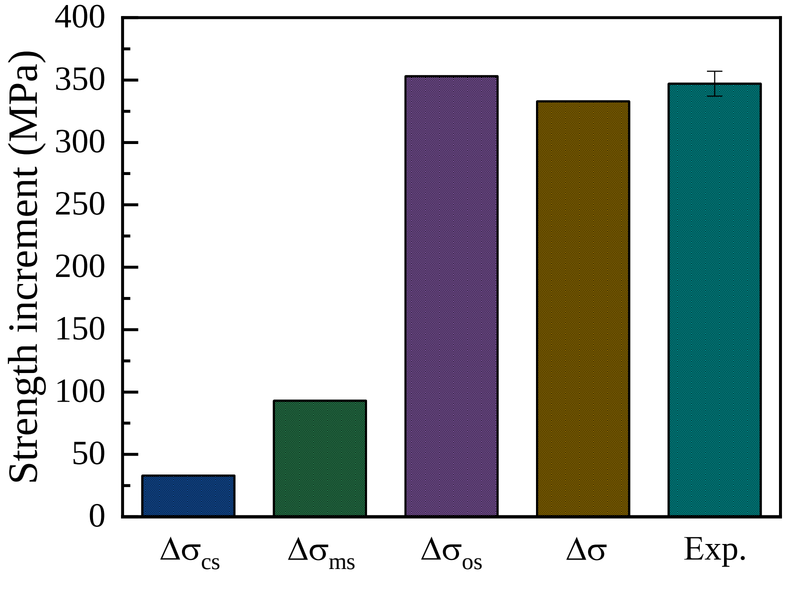

Fig. 14. Strengthening contributions of the $L1_2$ nanoparticles from coherency strengthening, modulus strengthening, and ordering strengthening. The experimental value is included for comparison.

5. Conclusions

This study investigated the thermodynamics and microstructural evolution of CNPs in a hierarchical-structured fcc/$L2_1$ HEA. The evolution sequences of the CNPs in both phases were systematically studied, and the precipitation and strengthening mechanisms were critically analyzed. The main conclusions are drawn as follows:

1. The as-homogenized alloy exhibits an fcc/$L2_1$ eutectic structure. Aging leads to the precipitation of $L1_2$ nanoparticles in the fcc phase and the precipitation of bcc nanoparticles in the $L2_1$ phase, thereby forming a multiple-phase hierarchical structure.
2. The formation of $L1_2$-type nanoparticles in the fcc phase occurs in two stages: first, the spinodal decomposition results in the formation of fcc nanoparticles enriched in Ni, Ti, and Al; second, as the nanoparticles grow, the structure ordering causes the transformation of the nanoparticles from the fcc to $L1_2$ structure.
3. The precipitation of bcc nanoparticles in the $L2_1$ phase also occurs in two stages: first, the spinodal decomposition of the $L2_1$ phase induces the formation of nanoparticles enriched in Cr and Fe, which maintain the $L2_1$ structure; second, as the nanoparticles grow, the increased enrichment of Cr and Fe promotes the transformation of the nanoparticles from the ordered $L2_1$ to disordered bcc structure.
4. Modeling of the strengthening mechanisms reveals that the precipitate shearing mechanism is operative for the $L1_2$ nanoparticles in the fcc phase, and the order strengthening of $L1_2$ nanoparticles plays a major role in enhancing the yield strength of the eutectic alloy. In contrast, the precipitation of bcc nanoparticles in the $L2_1$ phase does not change the strengthening efficiency of the $L2_1$ phase in the alloy, and thus, the strengthening contribution from the precipitation of bcc nanoparticles can be negligible.

Acknowledgements

Z.B.J. acknowledges the financial support from National Natural Science Foundation of China (52171162), Research Grants Council of Hong Kong (ECS 25202719, GRF 15227121, C1017–21GF, and C1020–21GF), Shenzhen Science and Technology

Program (JCYJ20210324142203009), Research Institute for Advanced Manufacturing Fund (P0041364 and P0046108), and PolyU Fund (P0038814, P0039624, P0042933, and P0043467). W.W. acknowledges the financial support from National Natural Science Foundation of China (52271122). H.W.Z. acknowledges the financial support from Liaoning Key Research and Development Program (2022JH2/101300080), the Chinese Academy of Sciences (ZDBS-LY-JSC023), the IMR Innovation Fund (2023-PY16), the National Natural Science Foundation of Liaoning Province (2023-BS-012).

References

[1] Y. Zhang, T.T. Zuo, Z. Tang, M.C. Gao, K.A. Dahmen, P.K. Liaw, Z.P. Lu, Microstructures and properties of high-entropy alloys, Prog. Mater. Sci. 61 (2014) 1-93.

[2] P. Sathiyamoorthi, H.S. Kim, High-entropy alloys with heterogeneous microstructure: Processing and mechanical properties, Prog. Mater. Sci. 123 (2022) 100709.

[3] Z. Li, S. Zhao, R.O. Ritchie, M.A. Meyers, Mechanical properties of high-entropy alloys with emphasis on face-centered cubic alloys, Prog. Mater. Sci. 102 (2019) 296-345.

[4] E.P. George, W.A. Curtin, C.C. Tasan, High entropy alloys: A focused review of mechanical properties and deformation mechanisms, Acta Mater. 188 (2020) 435-474.

[5] L. Liu, Y. Zhang, J. Han, X. Wang, W. Jiang, C.T. Liu, Z. Zhang, P.K. Liaw, Nanoprecipitate-strengthened high-entropy alloys, Adv. Sci. 8(23) (2021) 2100870.

[6] C. Varvenne, A. Luque, W.A. Curtin, Theory of strengthening in fcc high entropy alloys, Acta Mater. 118 (2016) 164-176.

[7] N. Ali, L. Zhang, D. Liu, H. Zhou, K. Sanaullah, C. Zhang, J. Chu, Y. Nian, J. Cheng, Strengthening mechanisms in high entropy alloys: A review, Mater. Today Commun. 33 (2022) 104686.

[8] Y. Lu, Y. Dong, H. Jiang, Z. Wang, Z. Cao, S. Guo, T. Wang, T. Li, P.K. Liaw, Promising properties and future trend of eutectic high entropy alloys, Scr. Mater. 187 (2020) 202-209.

[9] B. Gwalani, S. Dasari, A. Sharma, V. Soni, S. Shukla, A. Jagetia, P. Agrawal, R.S. Mishra, R. Banerjee, High density of strong yet deformable intermetallic nanorods leads to an excellent room temperature strength-ductility combination in a high entropy alloy, Acta Mater. 219 (2021) 117234.

[10] C. Zhang, C. Zhu, P. Cao, X. Wang, F. Ye, K. Kaufmann, L. Casalena, B.E. MacDonald, X. Pan, K. Vecchio, Aged metastable high-entropy alloys with heterogeneous lamella structure for superior strength-ductility synergy, Acta Mater. 199 (2020) 602-612.

[11] Q. Wang, Z. Li, S. Pang, X. Li, C. Dong, P.K. Liaw, Coherent precipitation and strengthening in compositionally complex alloys: a review, Entropy 20(11) (2018) 878.

[12] L. Fan, T. Yang, Y. Zhao, J. Luan, G. Zhou, H. Wang, Z. Jiao, C.-T. Liu, Ultrahigh strength and ductility in newly developed materials with coherent nanolamellar architectures, Nat. Commun. 11(1) (2020) 6240.

[13] Z. Fu, L. Jiang, J.L. Wardini, B.E. MacDonald, H. Wen, W. Xiong, D. Zhang, Y. Zhou, T.J. Rupert, W. Chen, E.J. Lavernia, A high-entropy alloy with hierarchical

nanoprecipitates and ultrahigh strength, Sci. Adv. 4(10) (2018) eaat8712.

[14] H.-L. Yi, D. Wei, R.-Y. Xie, Y.-F. Zhang, H. Kato, A strategy for enhancing the mechanical property of the precipitation-strengthened medium-entropy alloy, Mater. Sci. Eng. A 819 (2021) 141390.

[15] X.H. Du, W.P. Li, H.T. Chang, T. Yang, G.S. Duan, B.L. Wu, J.C. Huang, F.R. Chen, C.T. Liu, W.S. Chuang, Y. Lu, M.L. Sui, E.W. Huang, Dual heterogeneous structures lead to ultrahigh strength and uniform ductility in a Co-Cr-Ni medium-entropy alloy, Nat. Commun. 11(1) (2020) 2390.

[16] F. Vogel, N. Wanderka, S. Matsumura, J. Banhart, Early stages of decomposition within the γ′ phase of a Ni–Al–Ti model alloy, Intermetallics 22 (2012) 226-230.

[17] Y.H. Wen, J.P. Simmons, C. Shen, C. Woodward, Y. Wang, Phase-field modeling of bimodal particle size distributions during continuous cooling, Acta Mater. 51(4) (2003) 1123-1132.

[18] Y.Q. Chen, E. Francis, J. Robson, M. Preuss, S.J. Haigh, Compositional variations for small-scale gamma prime (γ′) precipitates formed at different cooling rates in an advanced Ni-based superalloy, Acta Mater. 85 (2015) 199-206.

[19] E.J. Mittemeijer, F. Sommer, Solid state phase transformation kinetics: a modular transformation model, Int. J. Mater. Res. 93(5) (2002) 352-361.

[20] D. Erdemir, A.Y. Lee, A.S. Myerson, Nucleation of Crystals from Solution: Classical and Two-Step Models, Acc. Chem. Res. 42(5) (2009) 621-629.

[21] h. Wendt, P. Haasen, Nucleation and growth of γ′-Precipitates in Ni-14 at.% Al, Acta Metall. 31(10) (1983) 1649-1659.

[22] X.S. Liu, R. Li, Y. Lu, Y.F. Zhang, P.F. Yu, G. Li, Spinodal decomposition induced nanoprecipitates strengthened CoCrNi-base medium entropy alloy, Mater. Sci. Eng. A 822 (2021) 141674.

[23] Y.J. Liang, L. Wang, Y. Wen, B. Cheng, Q. Wu, T. Cao, Q. Xiao, Y. Xue, G. Sha, Y. Wang, Y. Ren, X. Li, L. Wang, F. Wang, H. Cai, High-content ductile coherent nanoprecipitates achieve ultrastrong high-entropy alloys, Nat. Commun. 9(1) (2018) 4063.

[24] L. Wang, L. Wang, S. Zhou, Q. Xiao, Y. Xiao, X. Wang, T. Cao, Y. Ren, Y.-J. Liang, L. Wang, Y. Xue, Precipitation and micromechanical behavior of the coherent ordered nanoprecipitation strengthened Al-Cr-Fe-Ni-V high entropy alloy, Acta Mater. 216 (2021) 117121.

[25] C. Niu, A.J. Zaddach, A.A. Oni, X. Sang, J.W. Hurt, J.M. LeBeau, C.C. Koch, D.L. Irving, Spin-driven ordering of Cr in the equiatomic high entropy alloy NiFeCrCo, Appl. Phys. Lett. 106(16) (2015) 161906.

[26] D.M. Collins, N. D’Souza, C. Panwisawas, C. Papadaki, G.D. West, A. Kostka, P. Kontis, Spinodal decomposition versus classical γ′ nucleation in a nickel-base superalloy powder: An in-situ neutron diffraction and atomic-scale analysis, Acta Mater. 200 (2020) 959-970.

[27] X.P. Tan, D. Mangelinck, C. Perrin-Pellegrino, L. Rougier, C.A. Gandin, A. Jacot, D. Ponsen, V. Jaquet, Spinodal decomposition mechanism of γ′ precipitation in a single crystal Ni-based superalloy, Metall. Mater. Trans. A 45(11) (2014) 4725-4730.

[28] Y. Lu, X. Gao, L. Jiang, Z. Chen, T. Wang, J. Jie, H. Kang, Y. Zhang, S. Guo, H. Ruan, Y. Zhao, Z. Cao, T. Li, Directly cast bulk eutectic and near-eutectic high entropy alloys with balanced strength and ductility in a wide temperature range, Acta Mater. 124 (2017) 143-150.

[29] F. He, Z. Wang, S. Niu, Q. Wu, J. Li, J. Wang, C.T. Liu, Y. Dang, Strengthening the CoCrFeNiNb0.25 high entropy alloy by FCC precipitate, J. Alloys Compd. 667 (2016) 53-57.

[30] H. Jiang, H. Zhang, T. Huang, Y. Lu, T. Wang, T. Li, Microstructures and mechanical properties of Co2MoxNi2VWx eutectic high entropy alloys, Mater. Des. 109 (2016) 539-546.

[31] T. Xiong, S. Zheng, J. Pang, X. Ma, High-strength and high-ductility AlCoCrFeNi2.1 eutectic high-entropy alloy achieved via precipitation strengthening in a heterogeneous structure, Scr. Mater. 186 (2020) 336-340.

[32] M. Wang, Y. Lu, T. Wang, C. Zhang, Z. Cao, T. Li, P.K. Liaw, A novel bulk eutectic high-entropy alloy with outstanding as-cast specific yield strengths at elevated temperatures, Scr. Mater. 204 (2021) 114132.

[33] J.S. Blázquez, N. García-Pinto, C.F. Conde, A simple phenomenological model to describe stability of homogeneous solid solutions in high entropy alloys from metallic bonding potential, Materialia 28 (2023) 101744.

[34] D. Farkas, A. Caro, Model interatomic potentials for Fe–Ni–Cr–Co–Al high-entropy alloys, J. Mater. Res. 35(22) (2020) 3031-3040.

[35] R. Fereidonnejad, A. Ostovari Moghaddam, M. Moaddeli, Modified embedded-atom method interatomic potentials for Al-Ti, Al-Ta, Al-Zr, Al-Nb and Al-Hf binary intermetallic systems, Comput. Mater. Sci. 213 (2022) 111685.

[36] C. Kittel, P. McEuen, Introduction to solid state physics, John Wiley & Sons, 2018.

[37] Y.-K. Kim, H.-K. Kim, W.-S. Jung, B.-J. Lee, Development and application of Ni-Ti and Ni-Al-Ti 2NN-MEAM interatomic potentials for Ni-base superalloys, Comput. Mater. Sci. 139 (2017) 225-233.

[38] S.-H. Oh, D. Seol, B.-J. Lee, Second nearest-neighbor modified embedded-atom method interatomic potentials for the Co-M (M = Ti, V) binary systems, Calphad 70 (2020) 101791.

[39] I.S. Wani, T. Bhattacharjee, S. Sheikh, P.P. Bhattacharjee, S. Guo, N. Tsuji, Tailoring nanostructures and mechanical properties of AlCoCrFeNi2.1 eutectic high entropy alloy using thermo-mechanical processing, Mater. Sci. Eng. A 675 (2016) 99-109.

[40] F. Otto, Y. Yang, H. Bei, E.P. George, Relative effects of enthalpy and entropy on the phase stability of equiatomic high-entropy alloys, Acta Mater. 61(7) (2013) 2628-2638.

[41] S. Dasari, A. Jagetia, A. Sharma, M.S.K.K.Y. Nartu, V. Soni, B. Gwalani, S. Gorsse, R. Banerjee, Tuning the degree of chemical ordering in the solid solution of a complex concentrated alloy and its impact on mechanical properties, Acta Mater. 212 (2021) 116938.

[42] D. Chen, F. He, B. Han, Q. Wu, Y. Tong, Y. Zhao, Z. Wang, J. Wang, J.-j. Kai, Synergistic effect of Ti and Al on L12-phase design in CoCrFeNi-based high entropy alloys, Intermetallics 110 (2019) 106476.

[43] J. Zhang, S. Xin, Y. Zhang, P. Guo, H. Sun, T. Li, C. Qin, Effects of Elements on the Microstructure and Mechanical Properties of AlCoCrFeNiTi High-Entropy Alloys, Metals 13(1) (2023) 178.

[44] L. Liu, Y. Zhang, G. Wu, Y. Yu, Y. Ma, J. Ma, I. Baker, Z. Zhang, The effect of Al/Ti ratio on the evolution of precipitates and their effects on mechanical properties for Ni35(CoCrFe)55AlxTi10−x high entropy alloys, J. Alloys Compd. 906 (2022) 164291.

[45] H.U. Fuchs, The dynamics of heat, Springer, 1996.

[46] J.E. Morral, Stability limits for ternary regular system, Acta Metall. 20(8) (1972) 1069-1076.

[47] J. Bohong, C. Meihua, W. Qing, X. Zuyao, Thermodynamical criterion of spinodal decomposition in ternary system, Acta Metall. Sin. (05) (1990) 79-85.

[48] X. Zhou, R. Darvishi Kamachali, B.L. Boyce, B.G. Clark, D. Raabe, G.B. Thompson, Spinodal Decomposition in Nanocrystalline Alloys, Acta Mater. 215 (2021) 117054.

[49] L. Li, Z. Li, A. Kwiatkowski da Silva, Z. Peng, H. Zhao, B. Gault, D. Raabe, Segregation-driven grain boundary spinodal decomposition as a pathway for phase nucleation in a high-entropy alloy, Acta Mater. 178 (2019) 1-9.

[50] A. Kwiatkowski da Silva, D. Ponge, Z. Peng, G. Inden, Y. Lu, A. Breen, B. Gault, D. Raabe, Phase nucleation through confined spinodal fluctuations at crystal defects evidenced in Fe-Mn alloys, Nat. Commun. 9(1) (2018) 1137.

[51] P. Fan, K.-C. Chou, A self-consistent model for predicting interaction parameters in multicomponent alloys, Metall. Mater. Trans. A 30(12) (1999) 3099-3102.

[52] J.B. Rosenholm, Solubility and interaction parameters as references for solution properties. I. Exceptional mixing and excess functions, Adv. Colloid Interface Sci. 146(1) (2009) 31-41.

[53] M.S. xxGhiorso, I.S.E. Carmichael, M.L. Rivers, R.O. Sack, The Gibbs free energy of mixing of natural silicate liquids; an expanded regular solution approximation for the calculation of magmatic intensive variables, Contrib. Mineral. Petrol. 84(2) (1983) 107-145.

[54] X. Liu, S. Hao, An analysis on interaction parameters of binary solid solutions, Calphad 17(1) (1993) 67-78.

[55] R. DeHoff, Thermodynamics in materials science, CRC Press, 2006.

[56] P. Nash, V. Vejins, W. Liang, The Al−Ni−Ti (Aluminum−Nickel−Titanium) system, Bull. Alloy Phase Diagrams 3(3) (1982) 367-374.

[57] K. Kadirvel, S.R. Koneru, Y. Wang, Exploration of spinodal decomposition in multi-principal element alloys (MPEAs) using CALPHAD modeling, Scr. Mater. 214 (2022) 114657.

[58] Q. Ding, Y. Zhang, X. Chen, X. Fu, D. Chen, S. Chen, L. Gu, F. Wei, H. Bei, Y. Gao, M. Wen, J. Li, Z. Zhang, T. Zhu, R.O. Ritchie, Q. Yu, Tuning element distribution, structure and properties by composition in high-entropy alloys, Nature 574(7777) (2019) 223-227.

[59] Y. Lu, L. Zhang, Y. Chen, Z. Chen, Y. Wang, Phase-field study for the pre-precipitation process of L12-Ni3Al phase in Ni–Al–V alloy, Intermetallics 38 (2013) 144-149.

[60] K. Shen, Z.M. Yin, T. Wang, On spinodal decomposition in ageing 7055 aluminum alloys, Mater. Sci. Eng. A 477(1-2) (2008) 395-398.

[61] J. Jung, G. Ghosh, G.B. Olson, A comparative study of precipitation behavior of Heusler phase (Ni2TiAl) from B2-TiNi in Ni–Ti–Al and Ni–Ti–Al–X (X=Hf, Pd, Pt, Zr) alloys, Acta Mater. 51(20) (2003) 6341-6357.

[62] T. Yang, S. Xia, S. Liu, C. Wang, S. Liu, Y. Zhang, J. Xue, S. Yan, Y. Wang, Effects of AL addition on microstructure and mechanical properties of Al CoCrFeNi High-entropy alloy, Mater. Sci. Eng. A 648 (2015) 15-22.

[63] C.-C. Tung, J.-W. Yeh, T.-t. Shun, S.-K. Chen, Y.-S. Huang, H.-C. Chen, On the elemental effect of AlCoCrCuFeNi high-entropy alloy system, Mater. Lett. 61(1) (2007) 1-5.

[64] K. Kadirvel, H.L. Fraser, Y. Wang, Microstructural design via spinodal-mediated phase transformation pathways in high-entropy alloys (HEAs) using phase-field modelling, Acta Mater. 243 (2023) 118438.

[65] A.J. Ardell, Precipitation hardening, Metall. Trans. A 16(12) (1985) 2131-2165.

[66] D.N. Seidman, E.A. Marquis, D.C. Dunand, Precipitation strengthening at ambient and elevated temperatures of heat-treatable Al (Sc) alloys, Acta Mater. 50(16) (2002)

4021-4035.

[67] H. Wen, T.D. Topping, D. Isheim, D.N. Seidman, E.J. Lavernia, Strengthening mechanisms in a high-strength bulk nanostructured Cu–Zn–Al alloy processed via cryomilling and spark plasma sintering, Acta Mater. 61(8) (2013) 2769-2782.

[68] J. Miao, C. Slone, S. Dasari, M. Ghazisaeidi, R. Banerjee, E.P. George, M.J. Mills, Ordering effects on deformation substructures and strain hardening behavior of a CrCoNi based medium entropy alloy, Acta Mater. 210 (2021) 116829.

[69] Z.G. Wang, W. Zhou, L.M. Fu, J.F. Wang, R.C. Luo, X.C. Han, B. Chen, X.D. Wang, Effect of coherent L12 nanoprecipitates on the tensile behavior of a fcc-based high-entropy alloy, Mater. Sci. Eng. A 696 (2017) 503-510.

[70] M. Vittori, A. Mignone, On the antiphase boundary energy of Ni3(Al, Ti) particles, Mater. Sci. Eng. 74(1) (1985) 29-37.

[71] W.H. Tian, C.S. Han, M. Nemoto, Precipitation of α-Cr in B2-ordered NiAl, Intermetallics 7(1) (1999) 59-67.

[72] S. Tavares, K. Yang, M.A. Meyers, Heusler alloys: Past, properties, new alloys, and prospects, Prog. Mater. Sci. 132 (2022) 101017.

[73] K. Ma, H. Wen, T. Hu, T.D. Topping, D. Isheim, D.N. Seidman, E.J. Lavernia, J.M. Schoenung, Mechanical behavior and strengthening mechanisms in ultrafine grain precipitation-strengthened aluminum alloy, Acta Mater. 62 (2014) 141-155.

[74] M.R. Ahmadi, E. Povoden-Karadeniz, K.I. Öksüz, A. Falahati, E. Kozeschnik, A model for precipitation strengthening in multi-particle systems, Comput. Mater. Sci. 91 (2014) 173-186.

[75] P. Hirsch, F. Humphreys, Physics of strength and plasticity, MIT Press, Cambridge, 1969.

[76] L. Brown, R. Ham, Strengthening methods in crystals, Applied Sci. 9 (1971).